Materials Science & Engineering A 891 (2024) 145919

Contents lists available at ScienceDirect

Materials Science & Engineering A

journal homepage: www.elsevier.com/locate/msea

Strong resistance to shear instability in multilayered metallic composites by nanoscale amorphous-BCC crystalline interfaces

Feng Qin [a,b], Feihu Chen [a,b], Junhua Hou [c], Wenjun Lu [c], Shaohua Chen [d], Jianjun Li [a,b,*]

[a] College of Mechanical and Electrical Engineering, Central South University, Changsha, 410083, Hunan, PR China
[b] State Key Laboratory of Precision Manufacturing for Extreme Service Performance, Central South University, Changsha, 410083, Hunan, PR China
[c] Department of Mechanical and Energy Engineering, Southern University of Science and Technology, Shenzhen, 518055, PR China
[d] Institute of Advanced Structure Technology, Beijing Institute of Technology, Beijing, 100081, PR China

ARTICLE INFO

Keywords:
Electron microscopy
Amorphous materials
Composites
Nanocrystalline materials
Grains and interfaces
Plasticity

ABSTRACT

Experiments have shown that high strength and high plastic stability are difficult to be simultaneously obtained in crystalline-amorphous layered composites. Here we report a complete suppression of plastic instability in a strong multilayered composite via nanoscale BCC Nb crystalline-amorphous CuNb interface architecting. Specifically, the size-dependent hardness and shear instability of the designed nanolayered composites are systematically investigated with individual layer thickness (h) ranging from 2 to 100 nm by nano/micro-indentation tests. A mechanics model is also proposed to quantify the shear instability. A non-monotonic shear instability behavior is revealed with decreasing h. When $h > 40$ nm, a cutting-like shear banding prevails in the composites and the shear instability reduces with decreasing h. Finally, a homogeneous plastic deformation without shear banding is achieved at h of 40 nm. For $h < 40$ nm, a kinking-like shear banding occurs in the composites and the shear instability increases with reducing h. Further theoretical analysis reveals a critical layer thickness for activating homogeneous deformation in the composites, i.e., 45 nm, above and below which the shear deformation would be dominated by cutting-like and kinking-like shear banding, respectively. The cutting-like shear banding is attributed to the propagation of the mature shear band formed in the amorphous phase that penetrates the crystalline layer. The homogeneous plastic deformation can be ascribed to the activation of the confined layer slip mechanism in the crystalline layer and the non-clustered shear transformation zones initiated in the amorphous layer. The kinking-like shear banding below 40 nm may originate from the cooperative kinking of the constituent layers with decreasing h. The potential advantage of the ductile BCC metals over FCC ones for suppression of shear instability in crystalline-amorphous composites is discussed based on the unique dislocation activities in nanoscale BCC crystals (e.g., self-multiplication and significant cross-slipping mechanisms). The present study sheds some light on designing strong and ductile crystalline-amorphous composites by selecting an appropriate BCC crystalline phase and an optimal interface spacing to eliminate plastic instability.

1. Introduction

Amorphous alloys, or metallic glasses (MGs), have attracted extensive attention during the past few decades because of their excellent mechanical properties, such as ultrahigh hardness, high fracture toughness, good elastic deformation ability and excellent wear resistance [1–3]. However, MGs usually exhibit nearly zero macroscopic tensile ductility at room temperature due to the formation of catastrophic shear banding within a narrow region [4], which extremely limits their structural applications [5]. A lot of efforts have been made to improve the tensile ductility of MGs. One promising route is to form the crystal-amorphous composite by embedding ductile crystalline phases into the glassy matrix [6,7], stacking crystalline and amorphous nanolayers [8,9], and architecting supra-nano-dual-phase structure [10,11]. These studies demonstrated that the tensile ductility of the MG composite can be increased to ~ 4–14 % through dislocation slip [8], phase transformation or twinning in the crystalline phase [6], and shear band (SB) multiplication in the amorphous phase [10].

In particular, crystalline/amorphous (C/A) nanolayered (NL) composites have attracted great scientific interests in recent years due to

* Corresponding author. College of Mechanical and Electrical Engineering, and State Key Laboratory of Precision Manufacturing for Extreme Service Performance, Central South University, Changsha, 410083, Hunan, PR China.
E-mail addresses: mejjli@csu.edu.cn, jianjunli.mech@hotmail.com (J. Li).

https://doi.org/10.1016/j.msea.2023.145919
Received 21 June 2023; Received in revised form 2 November 2023; Accepted 12 November 2023
Available online 18 November 2023
0921-5093/

their excellent performance in overcoming the strength-ductility trade-off [12]. The pioneering work was carried out by Wang et al. [8], who synthesized a 35 nm crystalline Cu/5 nm amorphous CuZr NL composite by magnetron sputtering. Surprisingly, the tensile ductility of the composite reached as high as 13.8 % in room temperature tensile tests and a high yield strength of ~1.1 GPa was obtained simultaneously. Similarly, Kim et al. [9] achieved a high tensile strength (2.513 GPa) and tensile deformability (4 %) in a sputtered 112 nm amorphous CuZr/16 nm crystalline Cu NL composite, which is about 3 times more deformable in terms of plastic strain than pure $Cu_{50}Zr_{50}$ MG. The tensile ductility of the mentioned Cu/CuZr NL composites is even far greater than the reported values (~1–3%) of crystalline/crystalline (C/C) NL composites, such as Al/Ti [13], Cu/Ag [14] and Cu/Nb [15].

Generally, the excellent tensile plasticity of the C/A composites can be attributed to two reasons. The first one is that the crystalline layer can constrain the deformation of the amorphous layer through dislocation activities which accommodate the kinetic energy carried by SBs generated in the amorphous layer [9]. The second one is that the C/A interface, as a special heterogeneous interface, is able to act as both an obstacle for dislocation movement to strengthen the materials and an effective site for emitting and absorbing dislocations [8], enabling a dynamic cycle in the generation and annihilation of dislocations and in turn enhanced plastic deformation in the composite.

So far, most studies have focused on C/A NL composites with face-centered-cubic (FCC) crystalline phases, such as Cu/CuZr [8,9,16,17], Cu/CuNb [18,19], Al/SiC [20–30], Cu/PdSi [31,32], and other systems [33,34], since the soft FCC crystalline layer can well restrict the strain localization of the amorphous layer and thus improve the deformability of C/A NL composites [9]. However, the introduction of a soft crystalline phase also brings two significant drawbacks. One is that the strength of these C/A NL composites is very limited and is difficult to reach that of the amorphous phase in most cases [18,35], and another one is the deformation incompatibility between the soft crystalline and amorphous constituent layers that induce severe plastic instability during micropillar compression and indentation [16,21,22,25,26,36]. The origin is that the soft crystalline phase dominates the deformation due to the strong mechanical contrast between the soft crystalline layers and the hard amorphous layers.

For example, Chawla et al. [21] have demonstrated that the plasticity of Al/SiC NL composites was mainly accommodated by the deformation of the Al layers due to the strength disparity between the two constituent phases, while the damage took place in the form of localized cracking in the SiC layers and void nucleation and growth in the Al layers under nanoindentation tests. Moreover, by finite element modeling, they revealed that a large stress contrast exists between the soft and hard layers during indentation, and that the observed high local tensile stress in both the radial and transverse directions is responsible for the cracking in the SiC layers and the void nucleation in the Al layers [21]. Furthermore, Sun et al. [22] performed a nanoindentation study in combination with a transmission electron microscopy (TEM) on the same system. Their results showed that kink bands were formed at the sites of large bending strains, leading to cracking in the brittle SiC layer. In addition, Chawla and his co-workers [25,26] reported strong extrusion of the soft Al layers in the same system through micropillar compression tests at both room and high temperatures. It was found that the plastic instability was initiated from the fracture of the SiC layer and then the catastrophic failure occurred once multiple SiC layers fractured when the pillar was no longer able to bear the applied load [25]. In addition, the significant extrusion of the soft phase was also detected in Cu/CuZr system with a larger layer thickness (>50 nm) during micropillar compression tests, which was attributed to the much higher deformation borne by the Cu layers than the amorphous CuZr layers [16]. Also, the strong extrusion of the Cu layers indicates a premature failure of the layered interfaces, as suggested by Li et al. [37,38].

The above-mentioned typical plastic instabilities (kink bands and SBs) have also been reported by the research group at Los Alamos National Laboratory in other C/C and C/A NL systems including Cu/Nb [39–44], Al/TiN [44] and Al/Si [45] composites under nanoindentation and micropillar compression. For example, Bhattacharyya et al. [39] proposed that in Cu/Nb system the nanoindentation would cause a stress concentration and rotate the constituent layers, which brings the appropriate slip system into an easy shear direction and suddenly causes shear instability. While in micropillar compression, the shear banding in Cu/Nb system is attributed to the collective rotation and sliding of the layers since the interface blocks the dislocation transmission [43]. Recently, Sahu et al. [45] studied the mechanical behavior of Al/amorphous Si NL composite by nanoindentation and micropillar compression. They found that the soft Al phase was preferentially thinned down in between the brittle Si phases due to the significant strength difference between the two constituent phases. SBs were observed in the localized regions of the thin Si layers, resulting in a catastrophic failure of the brittle Si layer. This finding is similar to the damage mode in the Al/SiC NL composites as discovered by Chawla et al. [21].

Therefore, choosing a suitable crystalline phase with high strength and profuse slip systems (e.g., Ta, Nb, Cr, etc. with body-centered cubic (BCC) lattice structure) to design high-performance C/A NL composites becomes a potential route to further enhance the strength of the C/A composites while simultaneously increasing the plasticity. One typical example is that the amorphous ZrCuTi/crystalline Ta NL composites exhibited better plasticity and higher yield strength compared with the monolithic amorphous ZrCuTi alloy under micropillar compression, as reported by Chou et al. [46]. Recently, through uniaxial tensile tests, Gu et al. [47] demonstrated that the cracks generated in amorphous $Zr_{61}Cu_{17.5}Ni_{10}Al_{7.5}Si_4$ alloy can be completely suppressed by the introduction of the crystalline Ta layer to form the C/A NL composites. The mentioned experimental works preliminary confirmed that the introduction of a BCC phase is a feasible way to design C/A NL composites with high strength and high plasticity. However, the studies about C/A composites with BCC crystalline phase are few and limited to the effect of the hard BCC crystalline layer (metal Ta) on the compression plasticity [46] or tensile plasticity [47] of the C/A composites. The relationship between the mechanical properties and the deformation mechanism of the C/A NL composites with BCC crystalline phase and the layer thickness of the component still lacks a systematic study. In addition, whether the relatively soft BCC crystalline layer (e.g., Nb) compared with Ta is still capable of suppressing the propagation of SBs in the MGs layers remains to be determined. The present work aims to answer these questions by investigating the size-dependent mechanical behavior of the C/A composite.

Here the BCC crystalline Nb-amorphous CuNb system is selected to architect the C/A NL composite. The main motivations are as follows: (1) The strength of Nb with BCC lattice is much larger than that of Cu with FCC lattice (e.g., the yield strength Nb film is about 78 % higher than that of Cu film, i.e., 1.6 GPa and 0.9 GPa for Nb and Cu films, respectively [48]), which makes Nb as a feasible choice of crystalline layer for developing high-strength C/A NL composites; (2) The introduction of the stronger crystalline layer reduces the mechanical contrast between the crystalline and amorphous layers, which is helpful to suppress the premature failure of the layered interfaces; (3) Previous research mainly focused on the binary amorphous system with negative mixing enthalpy (such as CuZr and PdSi). The binary amorphous systems with positive mixing enthalpy (such as CuNb) are rarely considered.

In this work, crystalline Nb/amorphous CuNb composites with layer thickness h varying from 2 to 100 nm were synthesized by magnetron sputtering. The size-dependent hardness and shear banding (shear instability) behavior of the composites were systematically studied by nano and micro-indentation tests, respectively. It was found that the hardnesses of composites increase with decreasing h, approaching a maximum (8.57 GPa) at h of a few nanometers (below 10 nm) and then exhibiting size independence. The maximum hardness of the composites is comparable to that of the amorphous component (8.45 GPa).

Intriguingly, our micro-indentation tests revealed a non-monotonic behavior of shear instability, that is, the degree of shear instability decreases as the layer thickness decreases at large h ($h > 40$ nm), but it increases with decreasing layer thickness at small h ($h < 40$ nm). The above non-monotonic size-dependent shear instability leads to homogeneous plastic deformation in the composites with a medium h ($h = 40$ nm).

2. Materials and experiments

The crystalline Nb/amorphous CuNb (Nb/a-CuNb) NL composites were deposited on Si (100) substrate with a natural oxide layer by direct current magnetron sputtering (PTL6S PVD system) at room temperature. The purity of the Cu and Nb targets used for deposition are 99.99 % and 99.95 %, respectively. The base pressure of the vacuum chamber was 5 $\times 10^{-5}$ Pa and an Ar pressure of 0.3 Pa was used during deposition. The power used for Cu and Nb targets were 67 W and 150 W, respectively, resulting in a deposition rate of 0.1355 nm/s for Cu and 0.1379 nm/s for Nb. The amorphous CuNb layer was deposited by co-sputtering the Cu and Nb targets. The target alloy composition is $Cu_{60}Nb_{40}$ (atomic fraction). A series of Nb/a-CuNb NL composites (h = 2, 5, 10, 20, 40, 65, 100 nm) were prepared. The thicknesses of the constituent layers in the composites are equal ($h = h_{Nb} = h_{a-CuNb}$). A Nb layer was deposited on the Si substrate as the first layer and an amorphous CuNb layer was as the cap layer in all composites. The total thickness of the composites with $h > 20$ nm is ~2 μm, while that with $h \leq 20$ nm is ~1.2 μm. Also, monolayer Nb and amorphous CuNb films with a total thickness of 1.2 μm were also prepared for comparison. The crystallographic orientation of the films was characterized by X-ray diffraction (XRD, Bruker Advance D8). The cross-sectional microstructures before and after deformation and the composition of all the composites were examined by using TEM and scanning TEM (STEM) on a Talos F200X G2.

The hardness and the elastic modulus of all the composites were measured by nanoindentation (Agilent G200, Berkovich tip with a radius of ~50 nm) by using the continuous stiffness measurement (CSM) mode with a constant strain rate of 0.05 s^{-1}. The maximum indentation depth was 350 nm. Six indentations were performed for each sample to obtain the average hardness and standard deviation. The size-dependent shear banding behavior of the Nb/a-CuNb composites was tested by microindentation (Shimadzu HMV-G20ST) at room temperature. A microindentation load of 50 g was applied with a holding time of 5 s. The morphology of all samples induced by microindentation was characterized by scanning electron microscopy (SEM, Tescan Mira 3). After microindentation tests, the TEM lamellae of the indented region of the deformed samples were prepared by focused ion beam milling (FIB, FEI Helios NanoLab 600i).

3. Results

3.1. Microstructure of Nb/a-CuNb composites

Fig. 1 shows the XRD patterns of the as-deposited Nb/a-CuNb composites with different h and the monolayer Nb and amorphous CuNb films. It can be clearly seen that the monolayer CuNb film shows typical amorphous characteristics with a wide hump diffraction (see the inset in Fig. 1). The amorphous hump in the $Cu_{60}Nb_{40}$ film appears at ~40°, which is close to the diffraction angle for the amorphous hump in amorphous $Cu_{50}Nb_{50}$ as reported by Fan et al. [18], i.e., ~39°. In principle, four diffraction peaks can be detected using XRD for polycrystalline Nb, i.e., (110) at ~ 39°, (200) at ~ 56°, (211) at ~ 70° and (220) at ~ 83°. It can be noted that the monolayer Nb film and all Nb/a-CuNb composites exhibit strong Nb (110) diffraction peaks, indicating that the films grow with a preferred (110) texture. No obvious (200) peak was observed at 56° may be attributed to the scarce (200) texture in the as-deposited Nb films, which can be confirmed by the selected area electron diffraction (SAED) patterns for the as-deposited

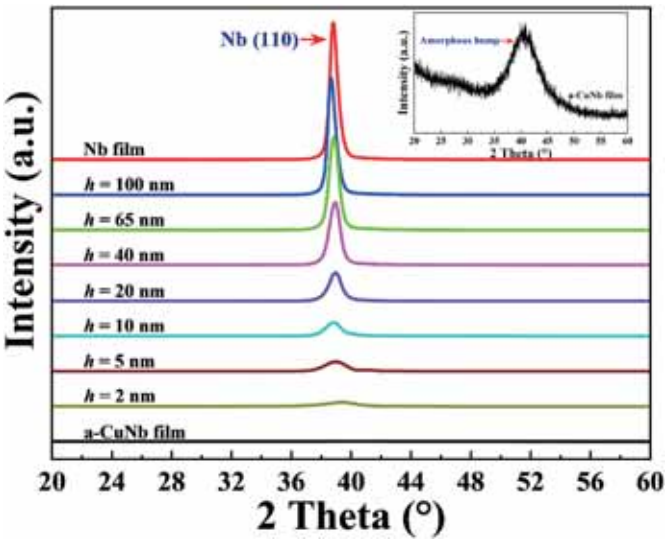

Fig. 1. XRD patterns of the Nb/a-CuNb NL composites with h varying from 2 to 100 nm and the monolayer Nb and amorphous CuNb films. All composites indicate a strong Nb (110) texture which is consistent with that detected in the monolayer Nb film. The inset shows a typical amorphous hump in the amorphous CuNb film.

Nb/a-CuNb samples, where the (200) texture diffraction spot is faint (see Supplementary Fig. 1). Similarly, only one Nb (110) peak was detected by 2θ diffraction range of 20°–60° in the as-deposited Cu/Nb NL composites [48]. In addition, the intensity of the (111) peak gradually decreases while the diffraction peaks gradually broaden with decreasing h, and the Nb (110) peak almost disappears at $h = 2$ nm and shows characteristics similar to that of the amorphous sample. The gradual broadening of the Nb (110) diffraction peak with the reduction of h can be attributed to the refined grain size in the crystalline Nb layers as h decreases.

The cross-sectional microstructures of the as-deposited Nb/a-CuNb NL samples were characterized by TEM as shown in Fig. 2. The representative bright-field TEM images of the samples with h = 100 nm (Fig. 2a), 40 nm (Fig. 2d) and 5 nm (Fig. 2g) show a modulated layer structure with clear interfaces. The SAED patterns in Fig. 2a, d, and 2g show a diffuse amorphous ring brought by the amorphous CuNb layer and a sharp bright spot of Nb (110), which are consistent with the XRD results. The corresponding high-angle annular dark field-STEM (HAADF-STEM) images (Fig. 2b, e and h) reveal that the columnar polycrystalline grains in Nb layer grow along the thickness direction. The high-resolution TEM (HRTEM) images of the samples with $h = 100$ nm, 40 nm and 5 nm are given in Fig. 2c, f and i, respectively, which definitely display the distinguishable interfaces of the C/A composites without intermixing. The fast Fourier transform (FFT) patterns of the white-framed position in the insets of Fig. 2c and f indicate the intrinsic crystalline and disordered structure for the Nb and the amorphous CuNb layers, respectively.

Based on the TEM observations, the measured individual layer thicknesses of Nb and amorphous CuNb layers and the grain size of the Nb layers of all samples (h = 2, 5, 10, 20, 40, 65, 100 nm) are presented in Table 1 and Fig. 3, respectively. It can be found that the actual thicknesses of the constituent layers are close to the nominal thickness. Besides, the grain size of crystalline Nb layers increases with increasing h (Fig. 3h). In particular, the grain size is smaller than the layer thickness at large layer thickness (Fig. 3a and b), whereas the grain size is consistent or slightly higher than the layer thickness in the composites with relatively small layer thickness (Fig. 3c–g). For example, the grain size is 76.8 ± 2.5 nm for $h = 100$ nm (Fig. 3a) and 64.6 ± 1.8 nm for h = 65 nm (Fig. 3b), whereas the grain size is 50.4 ± 0.7 nm for $h = 40$ nm (Fig. 3c) and 11.3 ± 0.3 nm for $h = 5$ nm (Fig. 3f). This statistical result

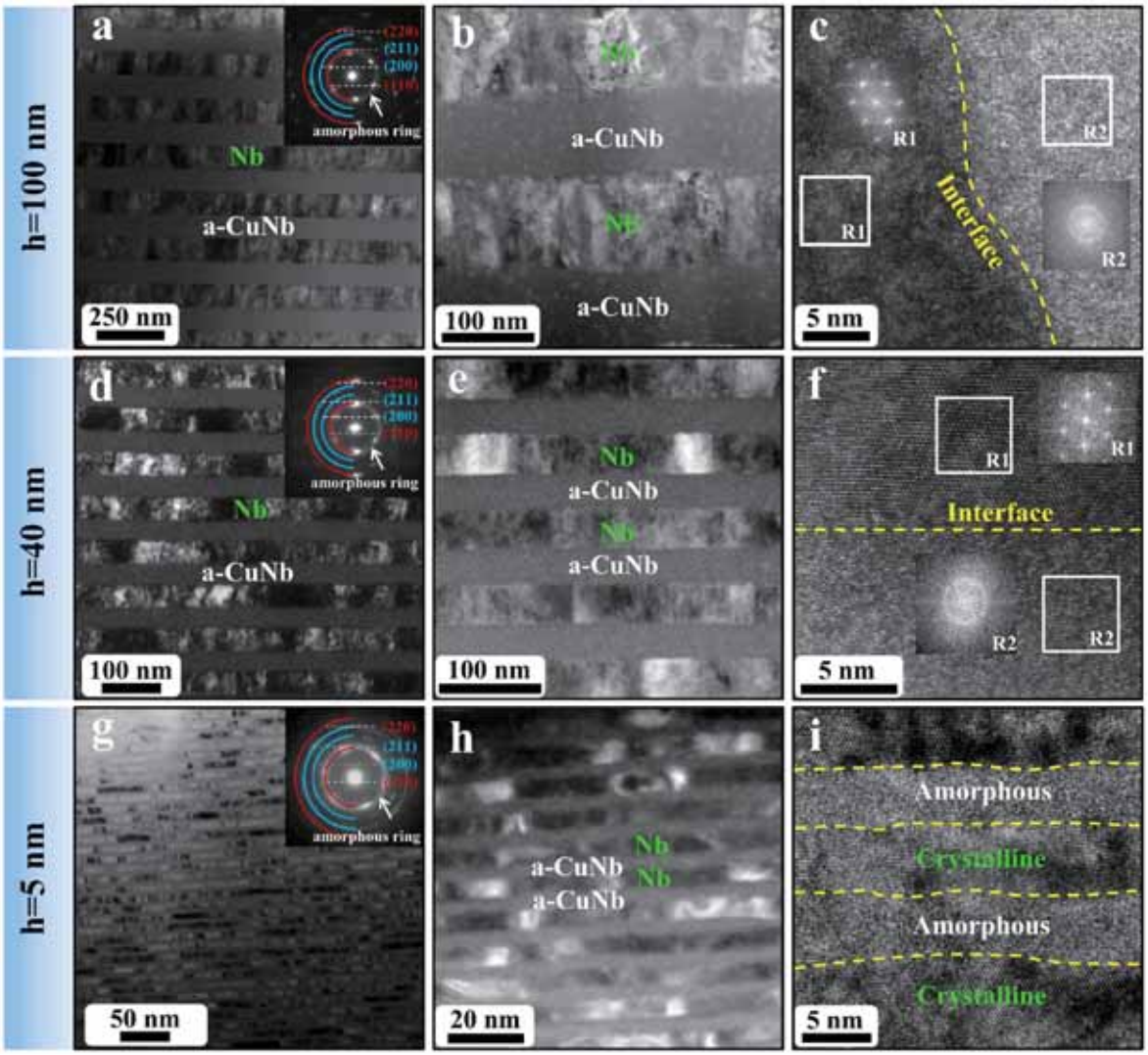

Fig. 2. Cross-sectional TEM micrographs of the as-deposited Nb/a-CuNb NL composites. (a) (d) and (g) are representative bright-field TEM images of the samples with h = 100 nm, 40 nm and 5 nm, respectively. The insets are the corresponding SAED patterns. (b), (e) and (h) are HAADF-STEM images of the corresponding samples. The HRTEM images of the samples with h = 100 nm (c), 40 nm (f) and 5 nm (i) show the interfacial structures between the Nb and the amorphous CuNb layers. The insets in (c) and (f) are the corresponding FFTs for both the crystalline Nb and the amorphous CuNb structures.

Table 1
The measured layer thicknesses of all Nb/a-CuNb samples.

Samples	Layer thickness (nm)	
	Nb	a-CuNb
h = 100 nm	92.8 ± 1.2	88.6 ± 2.0
h = 65 nm	63.2 ± 2.5	59.9 ± 2.7
h = 40 nm	39.1 ± 1.1	36.2 ± 1.0
h = 20 nm	20.8 ± 1.1	17.1 ± 1.1
h = 10 nm	10.2 ± 0.7	8.2 ± 0.5
h = 5 nm	4.7 ± 0.4	4.1 ± 0.5
h = 2 nm	2.8 ± 0.3	1.5 ± 0.2

suggests that the grain size in the as-deposited Nb/a-CuNb NL composites is strongly dependent on and constrained by the thickness of the constituent layer.

3.2. The hardness of the Nb/a-CuNb composites

Fig. 4a and b presents the hardness (H) and modulus (E) of the Nb/a-CuNb composite, the monolayer Nb and amorphous CuNb films as a function of the indentation depth, respectively. The hardness curves of all Nb/a-CuNb samples show a similar trend, i.e., the hardness decreases rapidly as the depth increases to ~50 nm due to the size effect of nanoindentation. Subsequently, the hardness reaches a nearly plateau region and does not change significantly with further penetration of the indenter. However, it can be found the hardness of the monolayer Nb film shows a remarkable increase after the plateau region (~50–150 nm). The observed increase in hardness can be attributed to the influence of the substrate because the Nb film is relatively soft that yields at a much smaller load compared to the Nb/a-CuNb composites and the amorphous CuNb film, resulting in an earlier substrate effect in the hardness-depth curves of the monolayer Nb film [49]. In contrast, the elastic modulus of all samples exhibits the same trend, i.e., increases slowly with increasing the indentation depth because of the effect of Si substrate with higher stiffness. According to Saha and Nix [49], the effect of the substrate hardness on the film hardness can be ignored in the case of soft films on hard substrates because the plastic deformation was contained only in the film before the indenter perpetrated to the substrate. Thereby, the average values of the plateaus in hardness-displacement curves can be adopted as the intrinsic hardness of the composites [49]. The modulus of the composites is calculated

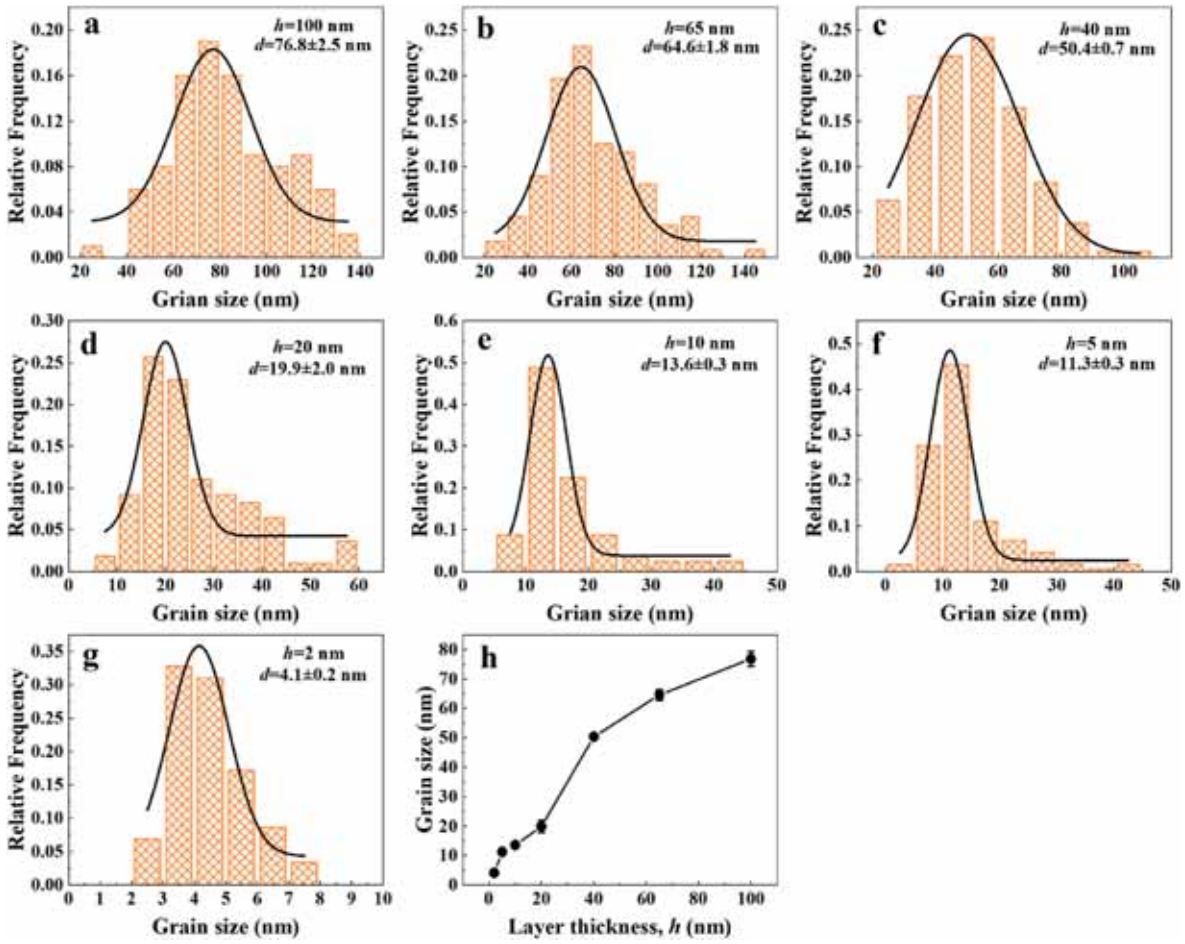

Fig. 3. The statistical distributions of the grain size in the crystalline Nb layers of the Nb/a-CuNb composites with different layer thicknesses *h*. (a–g) $h = 100$, 65, 40, 20, 10, 5 and 2 nm samples, respectively. (h) The variation of average grain size *d* with *h*.

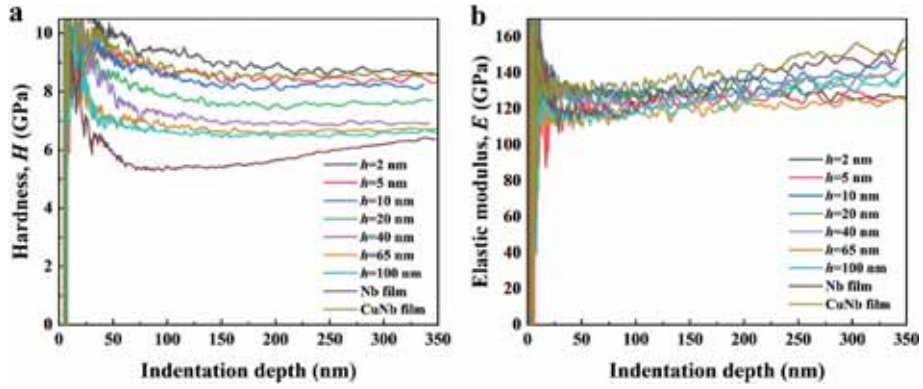

Fig. 4. Representative indentation depth dependent nano-hardness (a) and modulus (b) in the Nb/a-CuNb composites of various layer thicknesses ($h = 100$, 65, 40, 20, 10, 5 and 2 nm). Those of the monolayer Nb and amorphous CuNb films are also included for comparison.

using the data in ~10 % indentation depth of the total film thickness (100–150 nm, in which depths the substrate effect is insignificant). The obtained hardness and elastic modulus of the Nb/a-CuNb composites are presented in Table 2. It can be seen that hardness increases significantly as *h* decreases from *h* 100 to 10 nm, indicating a strong size effect. However, the hardness only shows a negligible change with the further reduction of the layer thickness to 2 nm, showing a size-independent behavior. The elastic modulus of the Nb/a-CuNb composites with different layer thicknesses does not vary significantly (Table 2).

To more clearly show the size-dependent strengthening effects of the Nb/a-CuNb with BCC/A system, the hardness as the function of $h^{-1/2}$ is plotted in Fig. 5. Besides, the hardnesses of other reported NL metallic composites, including X/Nb systems (X = Cu [50], Ag [51], Al [52], and Mg [53]), FCC/A (Cu/a-CuNb [18], Cu/a-CuZr [54]) and HCP/A (Zr/a-CuZr [55]) systems, are presented for comparison. First, it can be noted the hardness of the Nb/a-CuNb composites reaches a peak plateau as *h* is reduced to 5 nm (8.57 GPa) which is even higher than that of the amorphous CuNb film (indicated by the red horizontal dashed line) and

Table 2
Nanoindentation measured hardness (H) and elastic modulus (E) of the Nb/a-CuNb composites in different layer thickness (h), those of the amorphous CuNb and Nb films are also included.

Samples	Nano-hardness, H (GPa)	Elastic modulus, E (GPa)
$h = 100$ nm	6.46 ± 0.15	116 ± 4
$h = 65$ nm	6.75 ± 0.10	116 ± 3
$h = 40$ nm	6.92 ± 0.09	122 ± 2
$h = 20$ nm	7.54 ± 0.14	127 ± 1
$h = 10$ nm	8.32 ± 0.23	130 ± 1
$h = 5$ nm	8.57 ± 0.14	125 ± 2
$h = 2$ nm	8.56 ± 0.13	127 ± 1
CuNb film	8.45 ± 0.15	129 ± 1
Nb film	5.44 ± 0.19	124 ± 3

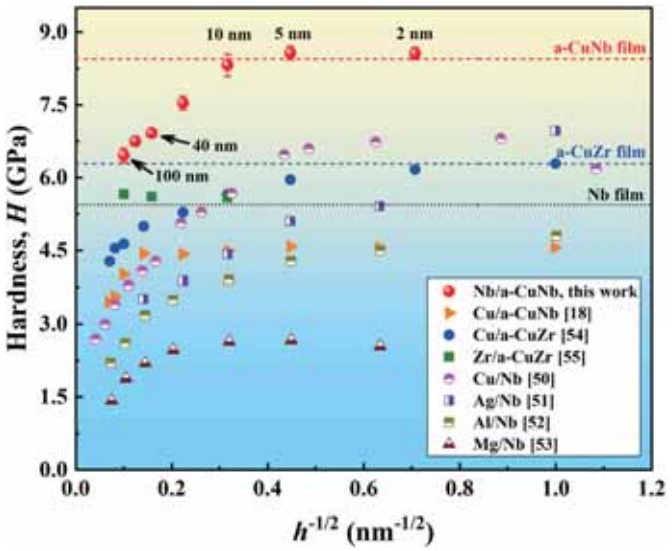

Fig. 5. Hardness of the Nb/a-CuNb composites as the function of $h^{-1/2}$. The hardness of FCC/A systems (Cu/a-CuNb [18], Cu/a-CuZr [54]), HCP/A (Zr/a-CuZr [55]), and X/Nb systems (X = Cu [50], Ag [51], Al [52], and Mg [53]) are also included for comparison.

much greater than the calculated value based on the rule of mixtures (ROM), $H_{ROM} = H_{a-CuNb}V_{a-CuNb} + H_{Nb}V_{Nb} = 6.95$ GPa, where V_{a-CuNb} and V_{Nb} are the corresponding volume fraction of the amorphous CuNb and Nb layers, respectively. This finding is similar to that observed in the Cu/a-CuZr [54] composites but is significantly different from the Cu/a-CuNb composites, the peak hardness of which is much lower than that of the amorphous CuNb film [18], as shown in Fig. 5. Second, compared with the C/C composites with X/Nb systems (e.g., Nb/Mg and Nb/Cu), the Nb/a-CuNb system shows no softening phenomenon, i.e., the strength decreases at the small h. Furthermore, compared with the C/A system (e.g. Zr/a-CuZr [55]), the Nb/a-CuNb composites show a much higher peak hardness. The higher peak hardness of the Nb/a-CuNb composites can be attributed to the higher hardness of the amorphous CuNb film (8.45 GPa) than the amorphous CuZr (6.49 GPa) films. Besides, unlike the Cu/a-CuNb composites reported by Fan et al. [18], which exhibit a weak strengthening effect, i.e., the hardness of the composites reaches a peak value at a large layer thickness ($h = 50$ nm) and does not increase further as h decreases, and the peak hardness is significantly lower than that of its hard phase, i.e., the amorphous CuNb layer. The authors attributed this unusual phenomenon in Cu/a-CuNb composites to the formation of a medium-range-ordered semi-crystalline structure in the amorphous CuNb layer near the C/A interface [18]. This medium-range order structure typically shows a middle peak in the XRD patterns as reported in Cu/a-CuNb [18] and Ag/Ni [56]. However, no obvious medium-range order interfacial layer is generated by atomic segregation or mutual solubility between the Nb and amorphous layers, which can be confirmed by the XRD results (Fig. 1) and the TEM images (Fig. 2). Thus, the interfaces of the present Nb/a-CuNb composites are definitely sharp, which might be responsible for the strong strengthening effect in the Nb/a-CuNb composites.

3.3. The shear instability of the Nb/a-CuNb composites

Fig. 6 shows typical morphologies of the Nb/a-CuNb composites with h varying from 100 to 2 nm after microindentation tests under a load of 50 g for 5 s. The indentation morphologies of the amorphous CuNb and Nb films are also presented for comparison. It can be found that a large amount of regular-shaped circular pileups occur on the indentation surface in the amorphous CuNb film, as denoted by the white arrows in Fig. 6a. It is generally believed that the circular-shaped pileups formed around the residual indent are induced by the formation of SBs in the internal of the materials [57,58]. The formation of abundant SBs represents the intrinsic brittleness of the amorphous solids as demonstrated by many experiments [4]. In contrast, there are only plastic pileups without SB in the Nb film (Fig. 6b), indicating a much better capability to resist shear instability (shear localization) than the amorphous film. For metallic multilayers, the circular-shaped pileups around the indent result from the accumulation of the shear deformation from the constituent layers along the shear stress direction [58]. Therefore, the more severe the shear deformation (shear instability), the more obvious the circular-shaped pileup would be around the indent. Then, it is clear from Fig. 6 that the shear banding behavior of the Nb/a-CuNb composites shows a strong size dependence and a non-monotonic resistance to shear instability as the layer thickness decreases from 100 to 2 nm. Specifically, the SEM images show that several SBs appear around the indentation surface of the composite with h of 100 nm, as marked by the white arrows in Fig. 6c and plotted in Fig. 7. When h decreases from 100 to 40 nm, the SB morphology changes from a circular shape to slightly wavy, as shown in Fig. 6c–e. This implies that the shear deformation becomes weaker, and that the shear instability of the composites is reduced as h decreases in the range of $h > 40$ nm. Note that the shear banding behavior becomes the weakest at $h = 40$ nm (Fig. 6e). Almost no SBs appear in the 40 nm sample. However, when h further reduces from 40 to 2 nm, the indentation-induced shear banding becomes more and more obvious (Fig. 6e–i), and the number of SBs is increased with decreasing the layer thickness (Fig. 7). For example, only two regularly shaped circular SBs are formed in the 20 nm sample. Yet, the number of SBs is increased to be as high as 6, 7 and 15 in the 10 nm, 5 nm and 2 nm samples, respectively, as illustrated in Supplementary Fig. 2. These circular SBs are similar to those in the C/C layered composites with small h [57]. The comparison of the indentation morphologies of the Nb/a-CuNb composites and that of the amorphous CuNb film show that the resistance to the shear instability of the former is much higher than the latter, indicating that the C/A structure with BCC crystalline phase is beneficial to reducing plastic instability. Especially, the above non-monotonic layer thickness dependence of the shear instability leads to an optimal resistance to shear instability in the composites with $h =$ 40 nm. Such phenomenon is distinctly different from the shear banding behavior of the C/C composites, where the shear instability increases with reducing h [36,59–61].

To explore the deformation inside the SBs of the Nb/a-CuNb composites, the cross-sectional TEM images of the composites with h of 100, 65, 40, 20 and 5 nm after microindentation tests were characterized. It can be noted that three SBs, here denoted by SB1, SB2 and SB3 as marked by the yellow dotted rectangles, are generated beneath the indentations of the 65 nm (Fig. 8b) and 100 nm (Fig. 8e) samples. The three SBs continuously cross through multi-constituent layers. Also, the end position of the SBs of the 100 nm sample is much closer to the Si substrate than that of the 65 nm sample, which indicates that the SBs of the former occurred a longer shear displacement in the composites than the latter. Besides, it can be found that the degree of the shearing and

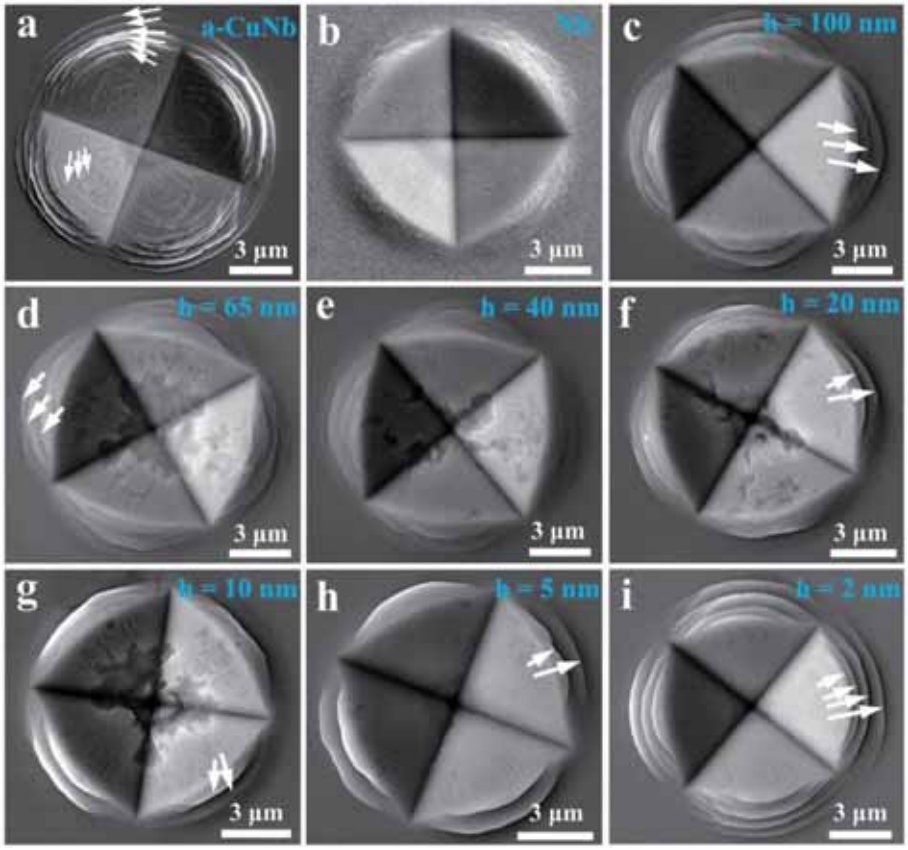

Fig. 6. SEM images of the microindentation morphologies of the monolayer amorphous CuNb film (a), the Nb film (b), and the Nb/a-CuNb composites with h of 100–2 nm (c–i). All films were indented under a load of 50 g for 5 s.

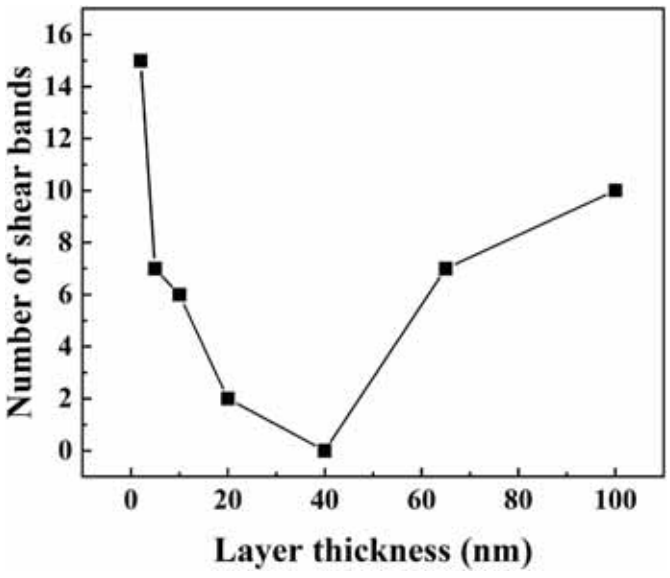

Fig. 7. The variation of the number of shear bands with the layer thickness.

twist of the kinked zone in the 65 nm sample is less than that of the 100 nm sample. Interestingly, the SBs of the composites with $h = 100$ nm and $h = 65$ nm share common features: (i) the layers of the SB region are kinked toward the squeezed direction resulting in a sharp twist, (ii) the originally flat interfaces are severely sheared to form sharp angles, which produces a highly concentrated deformation in a narrow region, as shown in Fig. 8c and f. This deformation is referred to as a cutting-like shear banding, which can be clearly recognized by the EDS mappings for the 100 nm sample (Fig. 8g).

Fig. 9 shows the cross-sectional TEM observation deformation of the 40 nm sample after microindentation of 50 g for 5s. Note that the constituent layers under the indenter exhibit homogeneous plastic deformation along the indentation radial direction without any shear banding (see Fig. 9b). The deformation topography of the constituent layer at higher magnification under microindentation also confirms the absence of shear banding (Fig. 9c and d). Furthermore, the plastic strain of each constituent layer under the indenter along the white arrow line in Fig. 9c is calculated by $(h-h_a)/h$, where h and h_a are the measured layer thickness before and after deformation, respectively. A minimum of 12 measurements for each layer were made in the deformed range of ~1 μm in Fig. 9c. It is interesting to observe that the plastic strains of the amorphous CuNb and Nb layers in the same bilayer periods are very close with the penetrate of the indenter, as shown in Fig. 9e. This means that the contribution of the hard amorphous CuNb layer to the overall deformation is comparable to that of the soft Nb layer, thus achieving a homogeneous plastic deformation.

To further confirm the homogeneous deformation that occurred in the 40 nm sample, additional micro-indentation tests were made using the same load of 50g. It can be seen that the morphologies of the micro-incidents (see Supplementary Fig. 3) produced by the new six independent tests are consistent with that in Fig. 9a. One of the newly produced micro-indents as a whole (Fig. 10a), instead of the half indent used in the TEM characterization (Fig. 9), was cross-sectioned by FIB and characterized by a field emission SEM. Some stepwise pileups can be observed around the indent (Fig. 10a), which is consistent with the morphology of the micro-indent in Fig. 9a. However, no obvious SBs are detected from the cross-sectional image and only some slight kink of the constituent layers occurs in the region near the sample surface

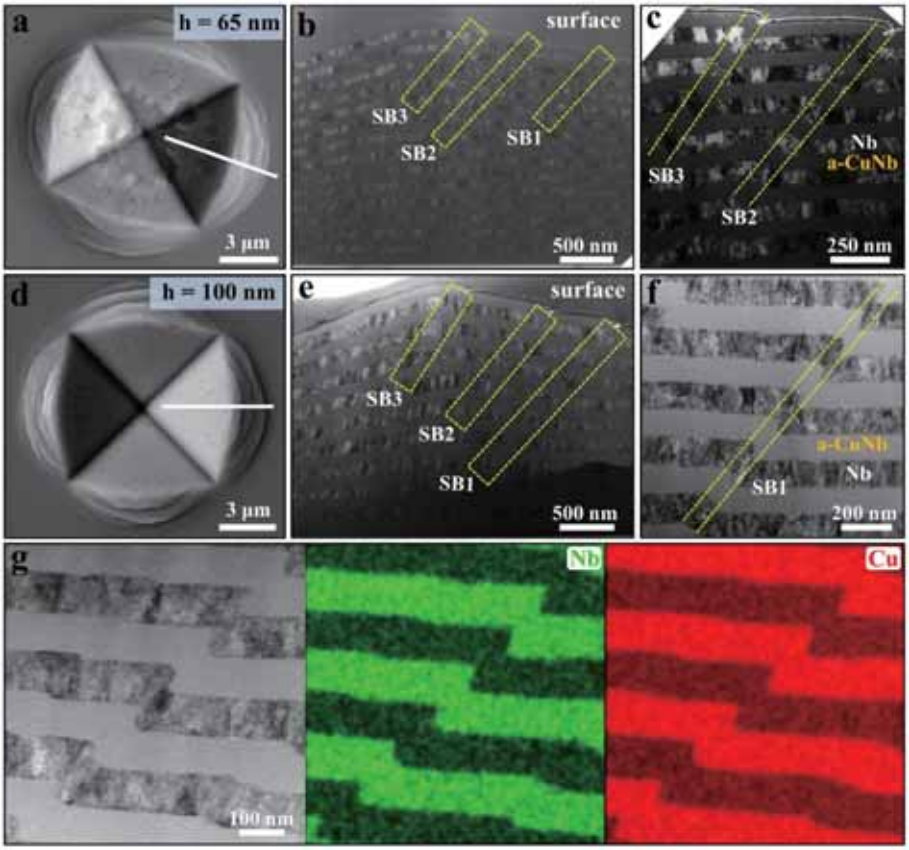

Fig. 8. Cross-sectional observations of the shear bands (SBs) in the Nb/a-CuNb samples with h of 65 and 100 nm. (a, d) Microindentation morphologies of the composites with $h = 65$ nm (a) and 100 nm (d) under a load of 50 g for 5s. (b, e) The corresponding cross-sectional TEM images, both of which show three SBs in the two samples. (c, f) The magnified images of the SBs from (b) and (e), respectively. (g) High magnification dark-field STEM image and the corresponding EDS mappings of the shear banding region for 100 nm sample, showing the sharply localized shearing deformation. The white lines in (a) and (d) designate where the cross-sectional TEM lamellae were taken.

(indicated by arrows in Fig. 10b and c). The slight kink is produced by the rotation of the constituent layers under the constraint of the conical indenter [39]. Thus, the observed stepwise pileups on the sample surface correspond to the slight kinking of the constituent layers near the sample surface, instead of SBs. It should be noted that the morphology of micro-indents in different tests may vary slightly but roughly the same as shown in Supplementary Fig. 3. Thus, the absence of similar kinks in the TEM characterization (Fig. 9b) can be attributed to ignorable pileups around the cross-sectioned half indent (Fig. 9a). The slight difference of the deformed microstructure between Figs. 9 and 10 comes from the very small variation of the different indents. Consequently, this result (Fig. 10) is qualitative consistent with the TEM observation shown in Fig. 9, which further evidences the strong suppression of shear banding at $h = 40$ nm.

The cross-sectional TEM images of the internal deformation of the Nb/a-CuNb composites with $h = 20$ nm and 5 nm after microindentation are presented in Fig. 11. It can be seen that two long SBs (marked by the yellow dotted rectangles) appear in the 20 nm sample (Fig. 11b), while one long SB and two short SBs are generated in the 5 nm sample (Fig. 11e). Furthermore, the TEM images of the longest SB of the 20 nm sample (Fig. 11c) and 5 nm sample (Fig. 11f) at higher magnifications show that the shear deformations of the two samples are similar, that is, the constituent layers are synergistically kinking along the shear direction and produce large shear displacements in the sheared region. This shear mode is named a kinking-like shear banding. This kink band has also been observed in thin film Al/SiC [21,22,29] and bulk Cu/Nb [44] NL composites under micropillar compression and nanoindentation. During micropillar compression, the Al/SiC and Cu/Nb composites are prone to form kink bands when the load direction is parallel or has a specific angle to the interface due to the large strength difference between the soft and hard layers. Moreover, Mayer et al. [30] suggested that kinking or buckling-mediated plasticity instability can be influenced by the geometry of the initial waviness of the interfaces as revealed by a microstructure-based three-dimensional finite element modeling. Note that the interfaces of the present Nb/a-CuNb composites are nearly perfectly flat planes (see Fig. 2), which is distinguished from the wavy interfaces as observed in the Al/SiC composites [30]. Besides, the kink band detected in the Al/SiC NL composites under both nanoindentation and micropillar compression leads to cracking in the brittle SiC layer [22,25]. This kink banding mechanism is totally different from those discovered in the Cu/Nb [44] and the present Nb/a-CuNb NL composites, in which the constituent layers exhibit a synergetic bending without cracking or voids formation, hence the lamellar structure of the material preserved and the interfaces maintain intact (Fig. 11g). These findings demonstrate that the shear banding behaviors of the samples with smaller layer thicknesses (i.e., $h = 5$ nm and 20 nm) are obviously different from those with larger layer thicknesses (e.g., $h = 100$ nm and 65 nm).

3.4. A mechanics model of quantifying the shear deformation

Microindentation results have revealed two shear banding modes in large and small layer thickness ranges, i.e., cutting-like shear banding (Fig. 8g) and kinking-like shear banding (Fig. 11g). Note that the layers within the SB gradually transform from slight kinking to sharply shearing from the bottom to top regions in the 100 nm sample (Fig. 12a),

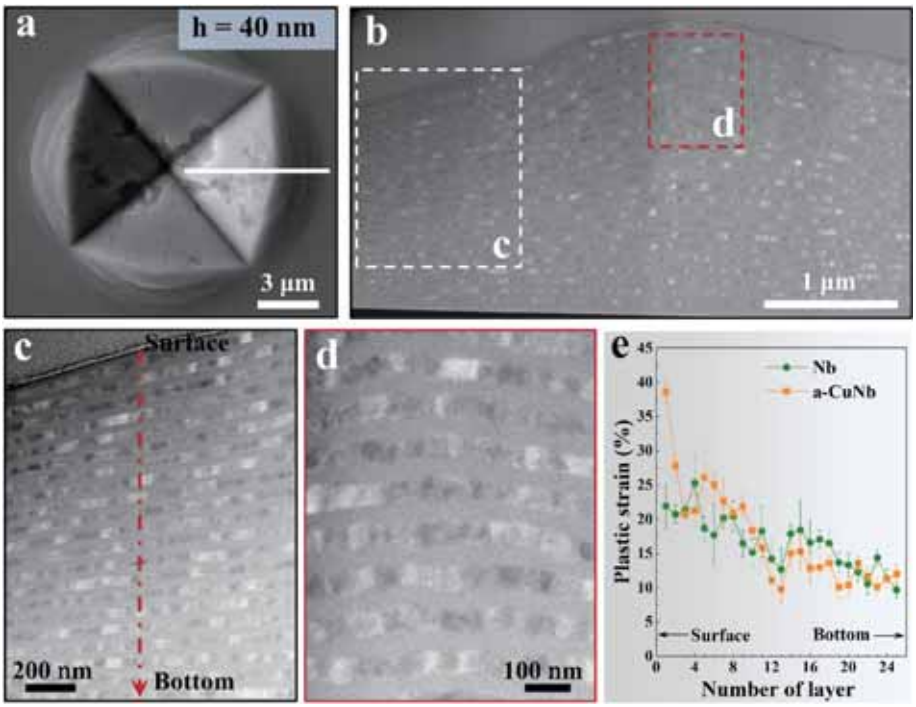

Fig. 9. (a) Microindentation morphology of the Nb/a-CuNb sample with h = 40 nm under a load of 50 g for 5 s. (b) Cross-sectional HAADF-STEM image of the indented region shows homogeneous plastic deformation. (c) Enlarged image of the compressed region as designated by the white box in (b). (d) Magnified observation of the pile-up area as designated by the red box in (b). (e) Plastic strain of each constituent layer along the arrow indicated in (c). The white line in (a) indicates where the cross-sectional TEM lamella was taken. (For interpretation of the references to colour in this figure legend, the reader is referred to the Web version of this article.)

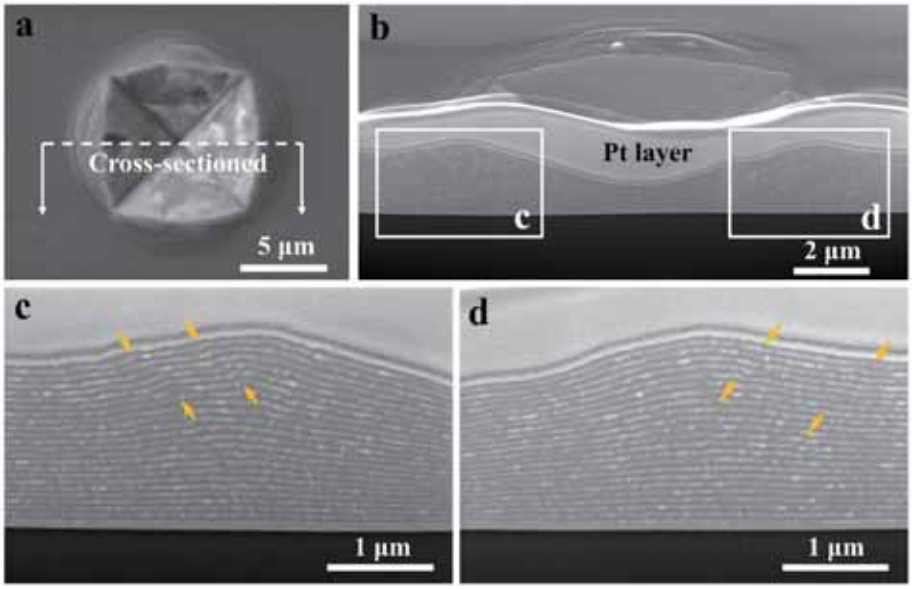

Fig. 10. The cross-sectional observation of the micro-indent after loading of 50 g in the Nb/a-CuNb sample with h = 40 nm. (a) SEM image of the morphology of the micro-indent. (b) Cross-sectional SEM image of the micro-indent. (c) and (d) The enlarged images of the regions as indicated by the white boxes in (b).

while the layers are always in the form of bending in the 5 nm sample (Fig. 12b). Although the shear banding modes are different in large and small layer thickness samples, the deformation that occurred inside the SB can both be considered to be mainly induced by shear stress given that the tilt angles of the SB formed in 100 nm (49°, Fig. 12a) and 5 nm (53°, Fig. 12b) samples are close to 45°, at which the shear stress reaches the maximum. Hence, to simplify and quantitatively compare the magnitude of the shear deformation of the Nb/a-CuNb composites with different layer thicknesses, a unified mechanics model (Fig. 12c and d) based on a pure shear stress state is proposed to describe the two shear banding modes.

Due to the nature of the layered stacking of the composite, the shear deformation within the SBs in NL composites results from the accumulation of shear deformation in each constituent layer. Thus a geometric model (Fig. 12c) of the SB is established firstly to analyze the deformation of each constituent layer within the SB [58]. Specifically,

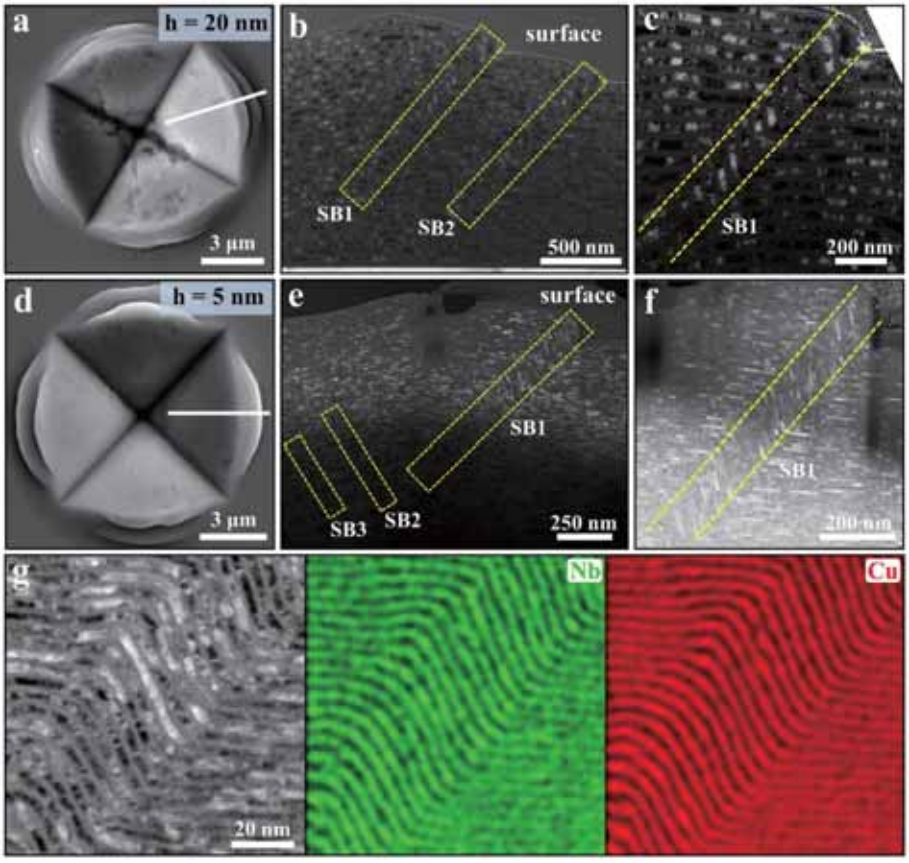

Fig. 11. Cross-sectional morphology of the shear bands (SBs) in the Nb/a-CuNb samples with h of 20 and 5 nm. (a, d) Microindentation morphologies of 20 nm (a) and 5 nm (d) samples under a load of 50 g for 5s. (b, e) The corresponding cross-sectional TEM images of the indented region show two SBs in the 20 nm sample (b) and three SBs in the 5 nm sample (e). (c, f) The magnified images of SB1 of the two samples. (g) High magnification dark-field TEM image and the corresponding EDS mappings of the shear banding region of the 5 nm sample, showing the multi-layer synergistic bending-induced SB. The white lines in (a) and (d) denote where the cross-sectional TEM lamellae were taken.

considering that the two types of SB generally exhibit similar geometrical features under pure shear stress, i.e., the kinking of multiple layers forms a narrow area with a specific width and angle, defined as the width of the SB (w_{SB}) and the tilt angle of the SB (α), respectively. The shear banding would induce a pile-up height on the surface as denoted by h_p. In addition, the kinking of the constituent layer gradually increases from the bottom to the surface region, which is denoted by the interface kink angle φ (ranging from 0° to $\pi - \alpha$), as indicated in the geometric model (Fig. 12c). It is assumed that the deformation of each layer can be represented by the stress and strain of the microelement adopted from the SB, schematically shown in Fig. 12d. Then the change of the right angle in the microelement represents the magnitude of the shear strain for the i-th layer (Nb or amorphous CuNb layer), i.e.,

$$\gamma_i = \beta - \beta' \tag{1}$$

Considering the geometry of the i-th deformed layer within the SB (Fig. 12c), it is easy to find that:

$$\gamma_i = \varphi_i + \alpha - \frac{\pi}{2} \tag{2}$$

Thus, the maximum shear strain within the SB is mainly determined by maximum φ. Then, the maximum shear strain within the SB can be written as:

$$\gamma_{max} = \varphi_{max} + \alpha - \frac{\pi}{2} \tag{3}$$

The calculated shear strain of each constituent layer inside the SB based on Eq. (2) is plotted in Fig. 13 for all samples. The positions of the constituent layers are normalized by L_i/L, where L_i denotes the position of the constituent layer with respect to the substrate while L indicates the total thickness of each sample. For the Nb/a-CuNb composites with internal SBs, only the strains of the SBs with significant shear deformation were calculated, i.e., three SBs (i.e., SB1, SB2 and SB3) in both 100 nm and 65 nm samples, two SBs (i.e., SB1 and SB2) in 20 nm sample and one SB (SB1) in 5 nm sample. Overall, the maximum shear strains of the constituent layers inside the SB for $h = 100$ and 65 nm samples are higher than that of the layers inside the SB for $h = 20$ and 5 nm samples as distinguished by the two shaded areas in Fig. 13, which demonstrates a more severe strain localization that occurred in samples with large layer thicknesses. Besides, one can find that the maximum shear strain of the 100 nm sample is higher than that of the 65 nm sample, while the shear strain in the 5 nm sample is slightly higher than the 20 nm sample, which indicates the non-monotonic size dependence of the shear deformation as observed in the indentation morphologies in Fig. 6.

Furthermore, in order to more clearly characterize the non-monotonic size-dependent shear deformation of the designed composites, the relationship between the degree of shear deformation and the typical geometric parameters generated by the shear banding, i.e., w_{SB} and h_p is analyzed in the following. First, it can be noted that the kinking of each constituent layer would induce a shear displacement along the shear banding direction (schematized in the enlarged region in Fig. 12c), which can be expressed by:

$$\Delta x_i = \frac{h_i}{\sin \alpha} \tag{4}$$

where h_i denote the pile-up height of the i-th layer. According to

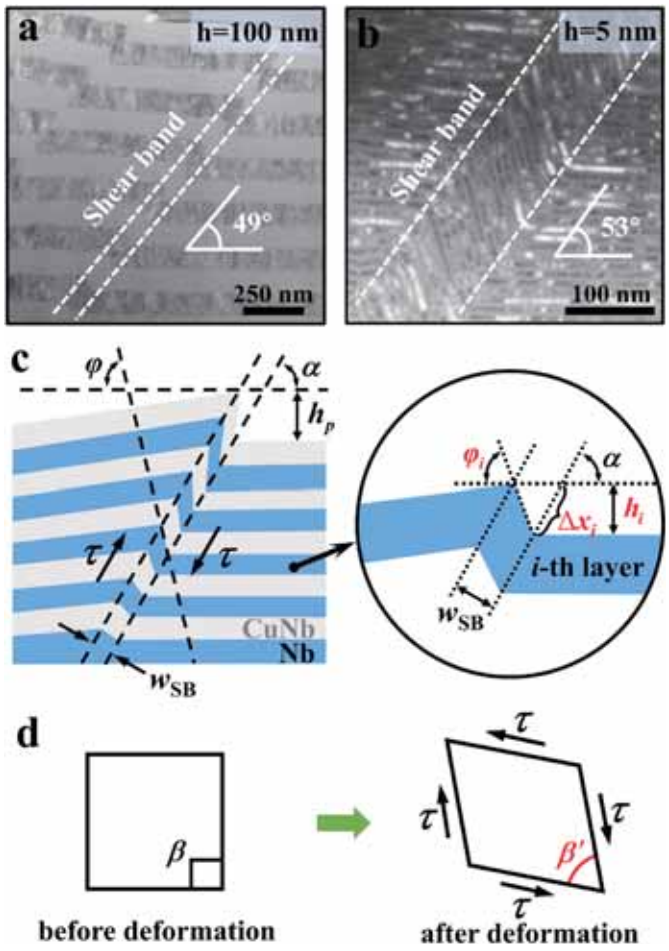

Fig. 12. Mechanics model of the deformation in the shear band (SB). (a, b) Cross-sectional HAADF-STEM images of the SB for the 100 nm (a) and 5 nm (b) samples, respectively. (c) Schematic diagram with parameter definitions of the SB, where w_{SB} is the width of the SB, h_p is the surface pile-up height within the SB, φ is the kink angle of the interface inside the SB, α is the tilting angle of the SB, h_i denotes the pile-up height in the i-th layer induced by the SB, and Δx_i represents the shear displacement of the i-th layer. (d) The pure shear stress state in the shear banding region, where β and β' indicate the right angle before and after deformation, respectively, as subjected to the shear stress.

geometric relation, the shear displacement for the i-th layer inside the SB can also be given by:

$$\Delta x_i = \frac{w_{SB}}{\tan(\pi-\alpha-\varphi_i)} + \frac{w_{SB}}{\tan\alpha} = \frac{w_{SB}\sin\varphi_i}{\sin\alpha\sin(\alpha+\varphi_i)} \tag{5}$$

Combining Eq. (4) and Eq. (5) yields:

$$\xi_i = \frac{h_i}{w_{SB}} = \frac{\sin\varphi_i}{\sin(\alpha+\varphi_i)} \tag{6}$$

Eq. (6) clearly shows that the ξ_i is the function of φ_i since α is a constant (~45°). Then by differentiating Eq. (6) with respect to φ_i we have

$$\frac{\partial(\xi_i)}{\partial(\varphi_i)} = \frac{\sin\alpha}{\sin^2(\alpha+\varphi_i)} \tag{7}$$

Note that the right term of Eq. (7) is always positive considering that the measured α and φ for all samples are in the range of (0, π/2) and (0, π − α), respectively, thus ξ_i is strictly monotonically increasing with respect to φ_i. The above analysis demonstrates that ξ_i is proportional to the magnitude of the interface kink angle φ, which is quite consistent with the relation between the shear strain γ and φ (Eq. (2)). Therefore, the

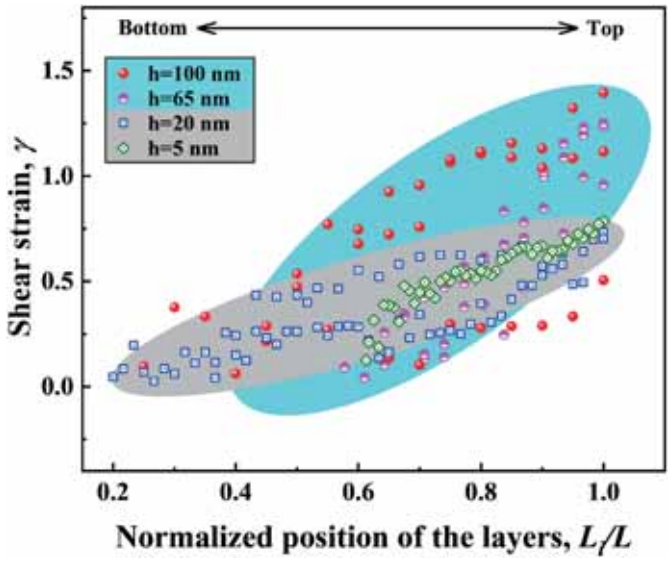

Fig. 13. Shear strain of the constituent layers within SBs of the Nb/a-CuNb composites with h of 100 nm, 65 nm, 20 nm and 5 nm.

magnitude of ξ_i can also be used to estimate the degree of shear deformation for the i-th layer, in addition to shear strain γ_i. Moreover, since the magnitude of φ is increased from the bottom to the top layer, and the pile-up height h_p induced by the SB corresponds to the pile-up height of the top layer, then the maximum value of h_i/w_{SB} is:

$$\xi_p = \frac{h_p}{w_{SB}} = \frac{\sin\varphi_{max}}{\sin(\alpha+\varphi_{max})} \tag{8}$$

The parameter ξ_p is able to represent the degree of the shear deformation for each SB.

As a consequence, the variation of SB width w_{SB}, surface pile-up height h_p and their ration $\xi_p = h_p/w_{SB}$ as well as γ_{max} with respect to the layer thickness h are summarized in Fig. 14. It can be found that the w_{SB} of the samples with larger layer thickness is smaller than that with smaller ones (Fig. 14a), which is consistent with the more severe deformation localization occurred in the former. Besides, the shear banding-induced surface pile-up height h_p first decreases and then increases with decreasing h, and reaches zero at $h = 40$ nm. This finding is consistent with the non-monotonic shear instability behavior as detected in Fig. 6. Moreover, it can be seen that the ξ_p is consistent with the maximum shear strain γ_{max}, and both in the 100 nm and 65 nm samples are higher than that in the 20 nm and 5 nm samples (Fig. 14c), which indicates a more severe deformation localization in samples with larger layer thicknesses. In contrast, the values of ξ_p in existing C/C composites (Cu/Au [57] and Cu/Cr [61]) show a monotonic decrease with the increase of the layer thickness, which is consistent with the monotonically increased shear instability with the decrease of the layer thickness, as reported in many C/C composites [36,59–61]. The above quantitative analysis further demonstrates the non-monotonic shear instability behavior of the Nb/a-CuNb composites. The proposed mechanics model gives a normalized parameter, i.e., ξ_p, to estimate the magnitude of the shear strain which is able to characterize the degree of shear instability of the NL metallic composites with different layer thicknesses, that is, the smaller value of this parameter, the less severe of the shear instability.

4. Discussion

4.1. Strengthening mechanism of the Nb/a-CuNb composites

Nanoindentation results have revealed (Fig. 5) that the hardness of

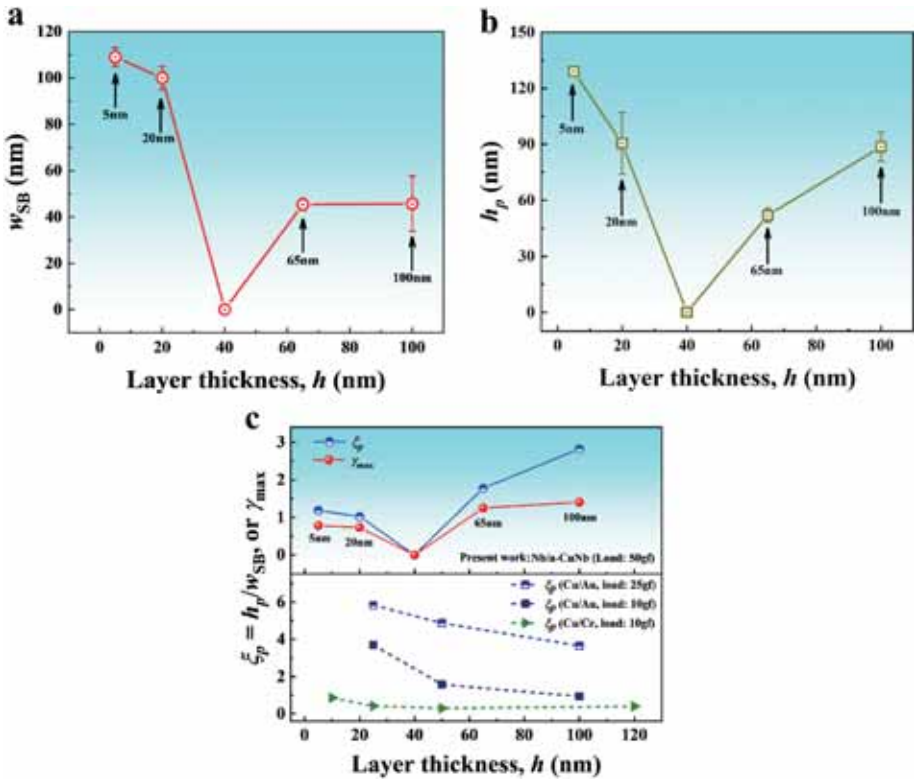

Fig. 14. (a) The measured SB width (w_{SB}) of samples with h = 100, 65, 40, 20 and 5 nm. (b) The surface pile-up height (h_p) induced by the shear banding. (c) The variation of ξ_p and γ_{max} with respect to the layer thickness. The data of the $\xi_p = h_p/w_{SB}$ detected in C/C composites (Cu/Au [57] and Cu/Cr [61]) are presented for comparison.

the Nb/a-CuNb composites increases with the decreasing layer thickness when $h \geq 10$ nm, and reaches a plateau value as $h < 10$ nm, showing a significant size effect between hardness and layer thickness. Thus, the potential strengthening mechanism of the Nb/a-CuNb composites will be analyzed and discussed in the subsection.

Unlike the traditional single-phase materials, the plastic deformation of which is accommodated through extensive dislocation nucleation and propagation events, the plastic deformation in NL metallic composites is typically governed by a few dislocation activities within the constituent layers constrained by the hetero-phase interfaces. Hall-Petch scaling law, $\sigma \propto h^{-1/2}$, has been frequently used to fit the strength of C/C metallic composites (e.g., Cu/Nb [50], Mg/Nb [53]), Cu/Zr [54]) with a large layer thickness ($h \geq 50$ nm) since the C/C interface has a strong barrier for dislocation transmission due to the difference of the lattice constant and the discontinuous slip system between the two constituent phases. However, for the C/A multilayers with a layer thickness of a few tens of nanometers, dislocation pileup is considered to be rare because the C/A interface acts as the natural dislocation sink, and the dislocation arriving at the interface is easily absorbed by the C/A interface [8,62]. For example, Wang et al. [8] have demonstrated that no dislocation pileup is observed in Cu layers of the 35 nm Cu/5 nm amorphous CuZr NL composites at any strains during tension tests. Furthermore, their simulations showed that the deformation process is mediated by the dislocation slip in a plane which is subsequently absorbed by the C/A interface. Thus, for the present Nb/a-CuNb composites, the confined layer slip (CLS) model [50] which involves the glide of a single Orowan-type dislocation bounded by two hetero-interfaces within the soft crystalline layers is used to described the strengthening behavior. Based on the CLS model, the stress required to drive a single dislocation glid in the Nb layer can be expressed as [50]:

$$\sigma_{\mathrm{CLS}} = M\frac{\mu b}{8\pi h'}\left(\frac{4-\nu}{1-\nu}\right)\left(\ln\frac{\alpha h'}{b}\right) - \frac{f}{h} + \frac{\mu b}{L(1-\nu)} \tag{9}$$

where $M = 3.06$ is the Taylor factor, b, ν and μ are the Burgers vector, Poisson ratio and shear modulus of the Nb layer, respectively, h' denotes the distance between adjacent interface parallel to the slip plane ($h' = h/\sin\theta$, where θ is the angle between (110) slip plane and interface, i.e., 60°), α is a parameter related to the width of dislocation core (α is in the range of 0–1 [50]), f is the characteristic interface stress of the NL composites (for C/A composites, f is adopted to be 0.5–1.1 J/m^2 [63]), L is the spacing between the interfacial dislocation arrays. Subsequently, it can be seen that the CLS model prediction shows a good agreement with the experimental data as $10 \leq h \leq 100$ nm (Fig. 15) by taking the parameters $M = 3.06$, $\mu = 44$ GPa (calculated based on the nanoindentation measured elastic modulus of Nb films), $b = 0.2858$, $\nu = 0.4$ [64], $\alpha = 0.12$, $f = 1.1$ J/m^2, and $L = 10.3$ nm. However, the CLS model prediction deviates significantly from the experimental values as $h < 10$ nm, in which the hardness exhibits almost size independence, i.e., the CLS mechanism is invalid at that scale.

Extensive researches [50,65] have suggested that the size-independent peak strength of the NL composites is determined by the barrier strength of the interface for slip transmission, behind which the physical mechanism is that a single dislocation developed in the composites can cross the interfaces. According to previous studies [66,67], the barrier strength of the interface for NL composites is determined by Koehler stress (τ_K) generated by the modulus difference of the two constituent phases, lattice parameter mismatch induced coherency stress (τ_c), the barrier stress associated with mismatch dislocation at the interface (τ_d), and the barrier stress originating from the difference in stacking faults energy (τ_{SFE}) of the component phases when stacking fault bounding the partials as the leading partial moves into the next constituent layer. Therefore, the barrier strength (τ_{IBS}) of the interface can be expressed as:

$$\tau_{IBS} = \tau_K + \tau_c + \tau_d + \tau_{SFE} \tag{10}$$

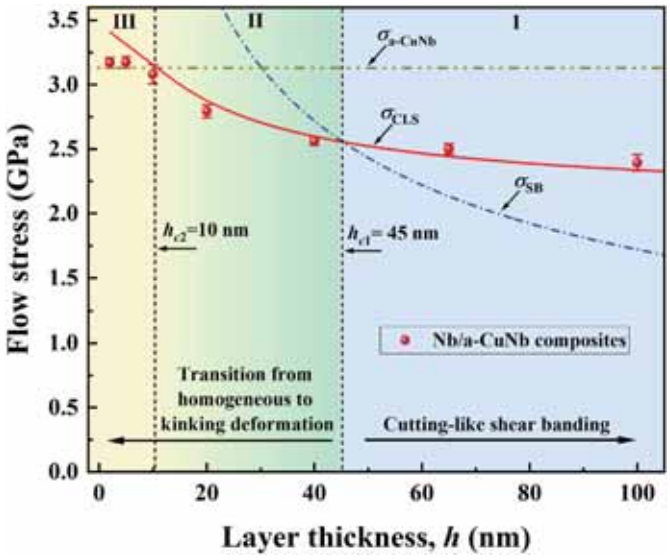

Fig. 15. The flow strength of the Nb/a-CuNb composites, estimated as the measured nano-hardness divided by a factor of 2.7, as a function of the layer thickness h. The CLS model (σ_{CLS}) is used to fit the strength of the samples with $10 \le h \le 100$ nm. The curve of σ_{SB} denotes the variation of the stress required for shear band (SB) propagation in the amorphous layer with its geometry characteristic size (here refer to layer thickness).

For the present Nb/a-CuNb C/A composites, τ_c, τ_d and τ_{SFE} can be ignored because (i) the C/A composites do not exist lattice mismatch between the crystalline and amorphous phases; (ii) there is absence of stable stacking faults in the BCC metals and the deformation is dominated by the motion of screw dislocations [68]. Thus, the barrier strength (τ_{IBS}) of the Nb/a-CuNb interface is mainly determined by the Koehler stress, which is expressed as [66]:

$$\tau_K = \frac{\mu_1(\mu_2 - \mu_1)\sin\theta}{(\mu_2 + \mu_1)8\pi} \tag{11}$$

where μ_1 and μ_2 are the shear modulus of the Nb and amorphous CuNb, respectively. θ is the smallest angle between the interface and the glide planes of the Nb layer, i.e., 60° for Nb (110). According to Wang et al. [69], the shear modulus of MGs can be estimated by dividing the elastic modulus by a factor of 2.61. Thus, μ_2 is calculated to be calculated to be 49.4 GPa by using the measured elastic modulus of the amorphous CuNb (129 GPa). As a consequence, $\tau_{IBS} = 0.088$ GPa, which corresponds to a normal stress of 0.27 GPa by multiplying a Taylor factor of 3.06. This value is significantly lower than the experimental peak strength (3.17 GPa) of the Nb/a-CuNb composites. This finding suggests that the C/A interface is relatively weak in resistance to dislocation transmission compared to C/C interfaces, and dislocation can easily approach the C/A interface and be absorbed due to the small image force [70].

In fact, the dislocation-dominated deformation in crystalline layers of the C/A composites may transform to STZs-dominated ones in the amorphous layer as the layer thickness h is decreased to several nanometers because the flow strength of the crystalline layer could be higher than that of the amorphous one at that scale, as suggested by Abboud et al. [55]. It can be found that with a further reduction of the layer thickness ($h < 10$ nm, see region III in Fig. 15), the crystalline Nb phase is stronger than the amorphous one since $\sigma_{CLS} > \sigma_{a-CuNb}$. Thus, the deformation of the composite is dominated by the amorphous phase instead of the crystalline Nb layers. Experiments have shown that the strength of the amorphous solids does not show an obvious size effect because of the nature of the disordered structure [71], which can be responsible for the size-independent peak strength/hardness for the Nb/a-CuNb composites at $h < 10$ nm.

4.2. The size-dependent shear banding behavior

Based on the microindentation results and the corresponding quantitative analysis on the shear deformation, an interesting size effects of the shear banding behavior have been found in the Nb/a-CuNb composites, i.e., (i) When h is larger than 40 nm, a cutting-like shear banding is formed in the composites (Fig. 8), and the degree of the shear instability decreases with decreasing h. (ii) Homogeneous plastic deformation appeared in the sample with medium layer thickness, i.e., 40 nm (Figs. 9 and 10). (iii) When h is less than 40 nm, shear instability in the form of kinking-like shear banding occurs in the composites (Fig. 11), and the degree of its shear instability increases as h decreases. These results indicate a non-monotonic shear instability behavior in the Nb/a-CuNb composites with decreasing h. Next, we provide a quantitative analysis and explanation for the experimental results that revealed a significant transition in the deformation modes related to the layer thickness in the Nb/a-CuNb composites.

4.2.1. Cutting like shear banding vs. homogeneous deformation

Recent simulation [62] suggests that the accommodation of plastic strain in C/A composites is initiated through the emission of dislocations near regions of the high atomic slip associated with STZs activity. With deformation processing, dislocations are absorbed into the amorphous layers via slip transfer across the C/A interface, which in turn activates more STZs in a correlated fashion near the C/A interface, a typical nucleation site of the embryonic SB [8,62,70]. Furthermore, experiments [71–73] have demonstrated that the stress required for SB formation and propagation in MGs is strongly dependent on their geometric size, e.g., the diameter of the micropillar and the thickness of the MGs. By analogy with Griffith's criterion for crack propagation, the critical stress required for a SB propagation is expressed as [71,72]:

$$\sigma_{SB} = \sqrt{\frac{2\sqrt{2}E\Gamma}{h}} \tag{12}$$

where E is the elastic modulus, Γ is the energy per unit area of SB, and h is the layer thickness. The value of Γ can be estimated by equating the work done on the SB to the increase in energy within the SB [72]. Previous study [74] suggested that the critical size for SB formation in MGs and the SB width belongs to the same length scale. Thus, here the critical size for SB formation in amorphous CuNb is adopted to be 30 nm based on the measured minimum SB width in the sample with $h = 100$ nm, which is in the range of the SB width for most MGs (10–100 nm) [75] and is close to the predicted minimum pillar diameter (~30 nm) for SB propagation in Zr-based MG [73]. By using the flow stress of the amorphous CuNb (3.13 GPa), $h = 30$ nm and $E = 129$ GPa, Eq. (12) yields $\Gamma = 0.81 \mathrm{Jm}^{-2}$, which is close to the Γ value (0.56 Jm^{-2}) for the Cu-based $Cu_{47}Ti_{33}Zr_{11}Ni_6Sn_2Si_1$ MG [71].

Consequently, the critical condition for SB formation in the Nb/a-CuNb composites is given by the intersection between the curves of σ_{CLS} and σ_{SB}, as plotted in Fig. 15, yielding a critical layer thickness (h_{c1}) of ~45 nm. This result indicates that at $h > 45$ nm the stress required for SB initiation in the amorphous phase is lower than that for CLS in the crystalline one, i.e., $\sigma_{SB} < \sigma_{CLS}$ (see region I in Fig. 15), hence SBs can initiate and propagate in the amorphous layer which eventually generates the cutting-like shear banding in the composites, as observed in the $h = 100$ and 65 nm samples (Fig. 8). This process is similar to the SB formation and propagation in metallic glasses [71]. If the layer thickness is decreased below a critical value, i.e., $h < 45$ nm, where the stress required for SB initiation in the amorphous phase is larger than that for CLS in the crystalline one, i.e., $\sigma_{SB} > \sigma_{CLS}$, the deformation of the composite is governed by the crystalline Nb layer in which CLS operates (see region II in Fig. 15). According to the findings of Misra et al. [76,77] in Cu/Nb layered composites, CLS can produce homogeneous deformation in the Nb layers. Simultaneously, the confined space in thin layers leads to homogeneous plastic flow in amorphous phases due to the

suppression of the SB formation as below a critical size (~30–100 nm) [72,73]. As a result, co-deformation occurs in the 40 nm sample (Fig. 9).

4.2.2. Homogeneous deformation vs. kinking like shear banding

The microindentation experiments have shown that kinking-like shear banding becomes predominant with the layers refining below 40 nm (Fig. 11). This kinking-like SB has also been observed in Cu/Au layered composites with layer thickness below 50 nm [57,61]. This transition from homogeneous deformation to kinking deformation is mainly attributed to the following two possible factors: (i) the two constituent phases are prone to shear with decreasing layer thickness; (ii) the C/A interfaces can slide easily in response to shear stress. With regard to the first scenario, it can be accepted that the dislocation activities and slip systems activated in the crystalline Nb layers would decrease gradually with the reduction of layer thickness. If a resolved shear stress favors one special slip system in the Nb layers, unbalanced slip activities within the layers can cause rotation of the layered interface plane [40]. The situation of the amorphous CuNb layer is different, which undergoes a homogeneous plastic flow at that scale. Thus, the amorphous layer is able to accommodate the rotation of the crystalline layers. Consequently, when the resolved shear stress along the interface reaches the stress necessary for plastic shear, kinking can occur through the cooperative rotation of the constituent layers (Fig. 16). This kinking is similar to the kink band formation in the 30 nm Cu/Nb NL composites as subject to a uniaxial compression stress parallel to the interface [44].

The second potential cause, interface sliding, may stimulate the kinking in C/A composites considering that the C/A interface has random structural variations, leading to interfacial regions with weak shear strengths that are susceptible to sliding [8]. If the interface plane is relatively weak in shear, the rotation could be sufficient for the resolved shear stress on the interface to facilitate interfacial slip [40]. Thus, the kink-like SB can be attributed to the unbalanced slip events-induced inhomogeneous deformation in those samples with small layer thickness, which leads to the rotation of the interface. This process is further facilitated by the easy sliding of the C/A interface with weak shear strength. Consequently, the increased shear instability as h decreases from 20 to 2 nm results from the degraded deformation ability of the crystalline layer because of the refined grain size and the increased interface intensity that promotes the cooperative kinking of the constituent layer. The critical size of this kink-like SB formation remains to be determined since the slip system within the polycrystalline layer is complex.

Based on the above discussions, it can be concluded that the combination of the size-dependent plasticity of the amorphous and crystalline layer leads to the strong size dependence of the shear banding behaviors of the Nb/a-CuNb composites. In particular, the homogeneous deformation achieved in Nb/a-CuNb composites is anticipated to be realized in other C/A composites by tunning the layer thickness of the BCC phase to trigger the CLS mechanism and controlling the layer thickness of the amorphous phase to induce uniform initiation of the STZs. It is emphasized that the thickness of the amorphous layer should not be too small, which would weaken its ability to absorb the incoming dislocations from the crystalline layer [78], possibly leading to inhomogeneous plastic deformation.

4.3. Effects of ductile BCC metals on the mechanical performances of C/A composites

Our microindentation experiments and the corresponding quantitative analysis reveal a non-monotonic shear instability behavior of the Nb/a-CuNb composites with decreasing layer thickness from 100 to 2 nm, resulting in a homogeneous deformation at $h = 40$ nm. This phenomenon has not been reported in FCC/A composites [16], which suggests the advantage of ductile BCC metals over FCC ones for suppression of shear instability in crystalline-amorphous composites.

Unlike the traditional FCC metals (e.g., Cu, Au), in which the dislocations can easily split into ribbons separated by stacking faults and the entire dislocation is constrained onto the same {111} planes preventing cross-slipping [79], there are no stable stacking faults in BCC metals, the plasticity behavior of BCC metals is controlled, to a large extent, by the motion of screw dislocations [68]. Since the core of screw dislocations is relatively compact, the preference to gliding on any particular system of slip planes is less distinct, resulting in the screw components of a dislocation loop are not restricted to any single glide plane and can therefore move in multi-planar to cross-slip processes [68,80]. Besides, by using molecular dynamics and dislocation dynamics simulations, Weinberger and Cai [81] demonstrated that a single dislocation nucleation event in BCC pillars is able to produce a much larger amount of plastic deformation than that in FCC pillars through the dislocation self-multiplication mechanism. Therefore, it can be speculated that despite very low initial dislocation densities present in both nanoscale FCC and BCC layers in the C/A composites, their evolution paths would be significantly different from each other. In FCC layers, mobile dislocations annihilate at the C/A interface upon the applied stress, causing

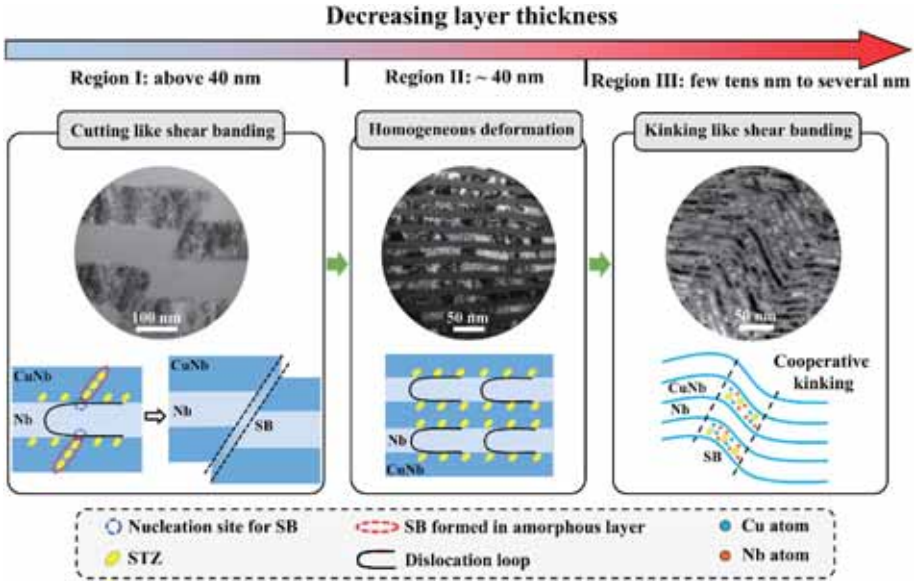

Fig. 16. Schematic illustration of the layer thickness-dependent deformation mechanism of the Nb/a-CuNb composites.

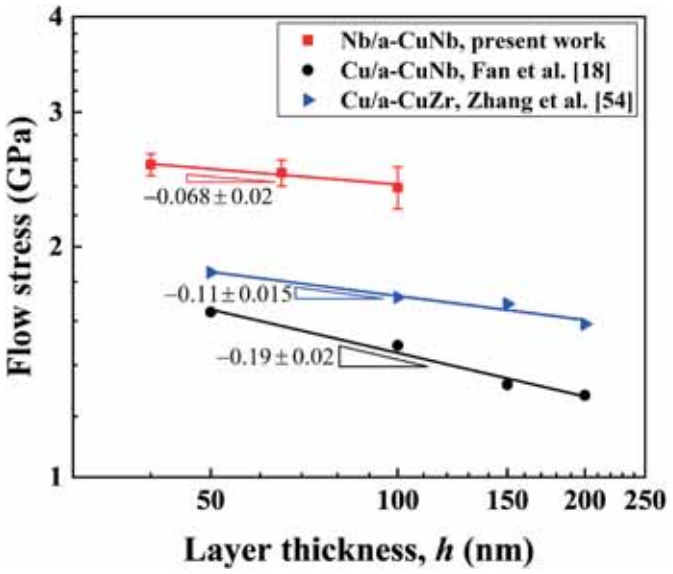

Fig. 17. The log-log plot of flow stress as a function of layer thickness h representing the scaling laws for BCC/A (Nb/a-CuNb) and FCC/A (Cu/a-CuNb [18], Cu/a-CuZr [54]) composites.

the overall dislocation density to decrease, and the associated increase in applied stress is further controlled by nucleation of new dislocation sources. This process of rapid dislocation emission and absorption is considered as a fundamental instability in plasticity at the nanoscale [82]. In BCC layers, however, a single dislocation can replicate itself and leave behind debris in response to the applied stress due to the self-multiplication mechanism in nanoscale BCC metals [81], which would enhance the resistance to plastic instability.

These different dislocation process between FCC and BCC metals generally results in a more significant increment in flow strength in FCC than BCC metals with the reduction of their geometric size (diameter of the nanopillar or layer thickness) [82], which can be confirmed by the log-log relation between the flow strength and the layer thickness for the present BCC/A (Nb/a-CuNb) and FCC/A (Cu/a-CuNb [18], Cu/-CuZr [54]) systems are plotted in Fig. 17. Here the data for these C/A composites is adopted with $h \geq 40$ to ensure that the flow strength is completely dominated by dislocation activity at that scale. It can be seen that both systems exhibit a power-law trend but a difference scaling slop, i.e., −0.068 for Nb/a-CuNb, −0.11 for Cu/a-CuNb, and −0.19 for Cu/a-CuNb composites, demonstrating that a more pronounced dislocation associated size strengthening effect in FCC/A than BCC/A composites, which is consistent the discussed dislocation mechanism before and agree well with the trend revealed in FCC and BCC nanopillar tests [82]. The higher absolute flow strength for BCC/A than FCC/A composites can be attributed to the higher lattice resistance to dislocation motion, i.e., Peierls stress, in BCC metals. Finally, based on the present experimental findings and discussions, a possible criterion for designing strong and ductile C/A composites can be captured, i.e., selecting a ductile BCC phase with a layer thickness of around tens nanometers (~40 nm) and refining the amorphous layer to prevent the formation of a mature SB to achieve both high strength and homogeneous plastic deformation.

5. Concluding remarks

In summary, a series of Nb/a-CuNb NL composites with various h (2–100 nm) were fabricated by magnetron sputtering. The size dependence of the hardness and shear instability behaviors of the composites were systematically investigated by nano and micro-indentations. A mechanics model has been proposed to quantify the shear instability of all the composites. The deformation mechanisms of the strong size dependence in the strengthening and resistance to shear instability are clarified. The main results are summarized as follows:

(1) The hardness of the Nb/a-CuNb composite as $h \geq 10$ nm can be well described by the CLS model based on the mechanism of single dislocation bowing out in the confined layer. At $h < 10$ nm, the hardness nearly reaches a plateau (8.57 GPa) and remains unchanged with the further decrease of h, which is comparable with the hardness of the amorphous CuNb film (8.45 GPa). Besides, compared with the FCC/A and HCP/A NL composites, the newly designed Nb/a-CuNb composites, i.e., BCC/A system, achieved a much higher peak hardness (8.57 GPa), which is 87 % and 53 % higher than the peak hardness of the Cu/CuNb and Zr/CuZr composites, respectively.

(2) Based on the microindentation tests, a non-monotonic shear banding behavior was observed in the Nb/a-CuNb composites with decreasing layer thickness. Two typical shear banding modes are detected. Specifically, a cutting-like shear banding was formed in the Nb/a-CuNb composite as $h > 40$ nm, which was associated with the formation and propagation of the SB initialized in the amorphous layer, and the degree of shear instability decreases with decreasing h in this region. The shear banding was completely suppressed in the Nb/a-CuNb composite with $h = 40$ nm which exhibited a homogeneous plastic deformation between constituent layers. This homogeneous deformation can be attributed to the activation of the CLS mechanism in the crystalline Nb layer and the uniformly distributed shear transformation zones in the amorphous CuNb layer. However, a kinking-like shear banding behavior was observed in the composites with $h < 40$ nm, and the degree of shear instability increases with decreasing h. This shear banding behavior is ascribed to the cooperative kinking of the constituent layers at a small thickness.

These findings may shed some light on the systematic and comprehensive understanding of the size-dependent mechanical properties of C/A NL composites and provide possible guidance for the design of novel composites with outstanding mechanical performance such as ultra-high strength and superior plasticity due to the significantly suppressed shear instability by tailoring the layer thicknesses of the constituent crystalline and amorphous phases.

Funding

The authors appreciate the financial supports from National Natural Science Foundation of China (NSFC) (Grant No. 12272413) and the Department of Science and Technology of Hunan Province, China (Grant No. 2021RC3022).

CRediT authorship contribution statement

Feng Qin: Methodology, Validation, Formal analysis, Investigation, Visualization, Writing – original draft. **Feihu Chen:** Investigation, Visualization. **Junhua Hou:** Investigation. **Wenjun Lu:** Investigation. **Shaohua Chen:** Writing – review & editing. **Jianjun Li:** Conceptualization, Resources, Project administration, Supervision, Funding acquisition, Writing – review & editing.

Declaration of competing interest

The authors declare that they have no known competing financial interests or personal relationships that could have appeared to influence the work reported in this paper.

Data availability

Data will be made available on request.

Appendix A. Supplementary data

Supplementary data to this article can be found online at https://doi.org/10.1016/j.msea.2023.145919.

References

[1] Y.Q. Cheng, E. Ma, Atomic-level structure and structure–property relationship in metallic glasses, Prog. Mater. Sci. 56 (2011) 379–473.
[2] C. Kuji, M. Mizutani, K. Shimada, K. Suzuki, H. Miura, T. Kuriyagawa, Evaluation of fracture properties of annealed Fe–Si–B–Cr amorphous alloys using micro-tensile tests and blanking machinability, Mater. Sci. Eng., A 848 (2022), 143483.
[3] C. Schuh, T. Hufnagel, U. Ramamurty, Mechanical behavior of amorphous alloys, Acta Mater. 55 (2007) 4067–4109.
[4] A.L. Greer, Y.Q. Cheng, E. Ma, Shear bands in metallic glasses, Mater. Sci. Eng. R Rep. 74 (2013) 71–132.
[5] M.F. Ashby, A.L. Greer, Metallic glasses as structural materials, Scripta Mater. 54 (2006) 321–326.
[6] Y. Wu, Y. Xiao, G. Chen, C.T. Liu, Z. Lu, Bulk metallic glass composites with transformation-mediated work-hardening and ductility, Adv. Mater. 22 (2010) 2770–2773.
[7] D.C. Hofmann, J.-Y. Suh, A. Wiest, G. Duan, M.-L. Lind, M.D. Demetriou, W. L. Johnson, Designing metallic glass matrix composites with high toughness and tensile ductility, Nature 451 (2008) 1085–1089.
[8] Y.M. Wang, J. Li, A.V. Hamza, T.W. Barbee, Ductile crystalline–amorphous nanolaminates, Proc. Natl. Acad. Sci. USA 104 (2007) 11155–11160.
[9] J.-Y. Kim, D. Jang, J.R. Greer, Nanolaminates utilizing size-dependent homogeneous plasticity of metallic glasses, Adv. Funct. Mater. 21 (2011) 4550–4554.
[10] G. Wu, K.C. Chan, L. Zhu, L. Sun, J. Lu, Dual-phase nanostructuring as a route to high-strength magnesium alloys, Nature 545 (2017) 80–83.
[11] C. Liu, Y. Liu, Q. Wang, X. Liu, Y. Bao, G. Wu, J. Lu, Nano-dual-phase metallic glass film enhances strength and ductility of a gradient nanograined magnesium alloy, Adv. Sci. 7 (2020), 2001480.
[12] B. Cheng, J.R. Trelewicz, Design of crystalline-amorphous nanolaminates using deformation mechanism maps, Acta Mater. 153 (2018) 314–326.
[13] D. Josell, D. van Heerden, D. Read, J. Bonevich, D. Shechtman, Tensile testing low density multilayers: aluminum/titanium, J. Mater. Res. 13 (1998) 2902–2909.
[14] H. Huang, F. Spaepen, Tensile testing of free-standing Cu, Ag and Al thin films and Ag/Cu multilayers, Acta Mater. 48 (2000) 3261–3269.
[15] N.A. Mara, D. Bhattacharyya, R.G. Hoagland, A. Misra, Tensile behavior of 40nm Cu/Nb nanoscale multilayers, Scripta Mater. 58 (2008) 874–877.
[16] J.Y. Zhang, G. Liu, S.Y. Lei, J.J. Niu, J. Sun, Transition from homogeneous-like to shear-band deformation in nanolayered crystalline Cu/amorphous Cu–Zr micropillars: intrinsic vs. extrinsic size effect, Acta Mater. 60 (2012) 7183–7196.
[17] W. Guo, E. Jägle, J. Yao, V. Maier, S. Korte-Kerzel, J.M. Schneider, D. Raabe, Intrinsic and extrinsic size effects in the deformation of amorphous CuZr/nanocrystalline Cu nanolaminates, Acta Mater. 80 (2014) 94–106.
[18] Z. Fan, S. Xue, J. Wang, K.Y. Yu, H. Wang, X. Zhang, Unusual size dependent strengthening mechanisms of Cu/amorphous CuNb multilayers, Acta Mater. 120 (2016) 327–336.
[19] N.A. Mara, D. Bhattacharyya, P. Dickerson, R.G. Hoagland, A. Misra, Layer thickness dependent strain rate sensitivity of Cu/amorphous CuNb multilayer, Appl. Phys. Lett. 92 (2008), 231901.
[20] X. Deng, N. Chawla, K.K. Chawla, M. Koopman, J.P. Chu, Mechanical behavior of multilayered nanoscale metal-ceramic composites, Adv. Eng. Mater. 7 (2005) 1099–1108.
[21] N. Chawla, D.R.P. Singh, Y.L. Shen, G. Tang, K.K. Chawla, Indentation mechanics and fracture behavior of metal/ceramic nanolaminate composites, J. Mater. Sci. 43 (2008) 4383–4390.
[22] P.L. Sun, J.P. Chu, T.Y. Lin, Y.L. Shen, N. Chawla, Characterization of nanoindentation damage in metal/ceramic multilayered films by transmission electron microscopy (TEM), Mater. Sci. Eng., A 527 (2010) 2985–2992.
[23] D.R.P. Singh, N. Chawla, Y.L. Shen, Focused Ion Beam (FIB) tomography of nanoindentation damage in nanoscale metal/ceramic multilayers, Mater. Char. 61 (2010) 481–488.
[24] G. Tang, Y.L. Shen, D.R.P. Singh, N. Chawla, Indentation behavior of metal–ceramic multilayers at the nanoscale: numerical analysis and experimental verification, Acta Mater. 58 (2010) 2033–2044.
[25] D.R.P. Singh, N. Chawla, G. Tang, Y.L. Shen, Micropillar compression of Al/SiC nanolaminates, Acta Mater. 58 (2010) 6628–6636.
[26] S. Lotfian, M. Rodríguez, K.E. Yazzie, N. Chawla, J. Llorca, J.M. Molina-Aldareguía, High temperature micropillar compression of Al/SiC nanolaminates, Acta Mater. 61 (2013) 4439–4451.
[27] S. Singh, C.S. Kaira, H. Bale, C. Huynh, A. Merkle, N. Chawla, In situ micropillar compression of Al/SiC nanolaminates using laboratory-based nanoscale X-ray microscopy: effect of nanopores on mechanical behavior, Mater. Char. 150 (2019) 207–212.
[28] C. Mayer, L.W. Yang, S.S. Singh, H. Xie, Y.L. Shen, J. Llorca, J. Molina-Aldareguia, N. Chawla, Orientation dependence of indentation behavior in Al–SiC nanolaminate composites, Mater. Lett. 168 (2016) 129–133.
[29] C.R. Mayer, L.W. Yang, S.S. Singh, J. Llorca, J.M. Molina-Aldareguia, Y.L. Shen, N. Chawla, Anisotropy, size, and aspect ratio effects on micropillar compression of AlSiC nanolaminate composites, Acta Mater. 114 (2016) 25–32.
[30] C.R. Mayer, J. Molina-Aladareguia, N. Chawla, Three dimensional (3D) microstructure-based finite element modeling of Al-SiC nanolaminates using focused ion beam (FIB) tomography, Mater. Char. 120 (2016) 369–376.
[31] A. Donohue, F. Spaepen, R.G. Hoagland, A. Misra, Suppression of the shear band instability during plastic flow of nanometer-scale confined metallic glasses, Appl. Phys. Lett. 91 (2007), 241905.
[32] I. Knorr, N.M. Cordero, E.T. Lilleodden, C.A. Volkert, Mechanical behavior of nanoscale Cu/PdSi multilayers, Acta Mater. 61 (2013) 4984–4995.
[33] Y. Wang, D. Kiener, X. Liang, J. Bian, K. Wu, J. Zhang, G. Liu, J. Sun, Constituent constraining effects on the microstructural evolution, ductility, and fracture mode of crystalline/amorphous nanolaminates, J. Alloys Compd. 768 (2018) 88–96.
[34] Y.F. Zhao, B. Chen, Y.Q. Wang, J.Y. Zhang, S.Z. Li, K. Wu, G. Liu, J. Sun, Size-dependent microstructural evolution and mechanical properties of crystalline/amorphous high-entropy alloy nanostructured multilayers: Cu/FeCoCrNiBSi vs Ni/FeCoCrNiBSi, Acta Mater. 246 (2023), 118706.
[35] J. Zhu, C. Gu, K.W. Xu, P. Huang, F. Wang, T.J. Lu, Effects of size and amorphous layer structure on the strength and plasticity of Cu/CuZr nanolaminates, Mater. Sci. Eng., A 738 (2018) 219–228.
[36] J.Y. Zhang, S. Lei, J. Niu, Y. Liu, G. Liu, X. Zhang, J. Sun, Intrinsic and extrinsic size effects on deformation in nanolayered Cu/Zr micropillars: from bulk-like to small-volume materials behavior, Acta Mater. 60 (2012) 4054–4064.
[37] J. Li, W. Lu, S. Zhang, D. Raabe, Large strain synergetic material deformation enabled by hybrid nanolayer architectures, Sci. Rep. 7 (2017), 11371.
[38] J. Li, W. Lu, J. Gibson, S. Zhang, S. Korte-Kerzel, D. Raabe, Compatible deformation and extra strengthening by heterogeneous nanolayer composites, Scripta Mater. 179 (2020) 30–35.
[39] D. Bhattacharyya, N.A. Mara, P. Dickerson, R.G. Hoagland, A. Misra, Transmission electron microscopy study of the deformation behavior of Cu/Nb and Cu/Ni nanoscale multilayers during nanoindentation, J. Mater. Res. 24 (2009) 1291–1302.
[40] N.A. Mara, D. Bhattacharyya, J.P. Hirth, P. Dickerson, A. Misra, Mechanism for shear banding in nanolayered composites, Appl. Phys. Lett. 97 (2010), 021909.
[41] N. Li, N.A. Mara, J. Wang, P. Dickerson, J.Y. Huang, A. Misra, Ex situ and in situ measurements of the shear strength of interfaces in metallic multilayers, Scripta Mater. 67 (2012) 479–482.
[42] I.J. Beyerlein, N.A. Mara, J.S. Carpenter, T. Nizolek, W.M. Mook, T.A. Wynn, R. J. McCabe, J.R. Mayeur, K. Kang, S. Zheng, J. Wang, T.M. Pollock, Interface-driven microstructure development and ultra high strength of bulk nanostructured Cu-Nb multilayers fabricated by severe plastic deformation, J. Mater. Res. 28 (2013) 1799–1812.
[43] S.J. Zheng, J. Wang, J.S. Carpenter, W.M. Mook, P.O. Dickerson, N.A. Mara, I. J. Beyerlein, Plastic instability mechanisms in bimetallic nanolayered composites, Acta Mater. 79 (2014) 282–291.
[44] T. Nizolek, N.A. Mara, I.J. Beyerlein, J.T. Avallone, T.M. Pollock, Enhanced plasticity via kinking in cubic metallic nanolaminates, Adv. Eng. Mater. 17 (2015) 781–785.
[45] B.P. Sahu, W. Wu, J. Wang, A. Misra, Deformation behavior of crystalline/amorphous Al-Si nanocomposites with nanolaminate or nanofibrous microstructures, Phys. Rev. Mater. 6 (2022), 094002.
[46] H.S. Chou, X.H. Du, C.J. Lee, J.C. Huang, Enhanced mechanical properties of multilayered micropillars of amorphous ZrCuTi and nanocrystalline Ta layers, Intermetallics 19 (2011) 1047–1051.
[47] C. Gu, F. Wang, P. Huang, K.W. Xu, T.J. Lu, Size-dependent hardness and tensile plasticity of Ta-Zr 61 Cu 17.5 Ni 10 Al l7.5 Si 4 nanolaminates, J. Alloys Compd. 707 (2017) 321–326.
[48] J.Y. Zhang, X. Zhang, R.H. Wang, S.Y. Lei, P. Zhang, J.J. Niu, G. Liu, G.J. Zhang, J. Sun, Length-scale-dependent deformation and fracture behavior of Cu/X (X=Nb, Zr) multilayers: the constraining effects of the ductile phase on the brittle phase, Acta Mater. 59 (2011) 7368–7379.
[49] R. Saha, W.D. Nix, Effects of the substrate on the determination of thin film mechanical properties by nanoindentation, Acta Mater. 50 (2002) 23–38.
[50] A. Misra, J.P. Hirth, R.G. Hoagland, Length-scale-dependent deformation mechanisms in incoherent metallic multilayered composites, Acta Mater. 53 (2005) 4817–4824.
[51] M.Z. Wei, J. Shi, Y.J. Ma, Z.H. Cao, X.K. Meng, The ultra-high enhancement of hardness and elastic modulus in Ag/Nb multilayers, Mater. Sci. Eng., A 651 (2016) 155–159.
[52] E.G. Fu, N. Li, A. Misra, R.G. Hoagland, H. Wang, X. Zhang, Mechanical properties of sputtered Cu/V and Al/Nb multilayer films, Mater. Sci. Eng., A 493 (2008) 283–287.
[53] B. Ham, X. Zhang, High strength Mg/Nb nanolayer composites, Mater. Sci. Eng., A 528 (2011) 2028–2033.
[54] J.Y. Zhang, Y. Liu, J. Chen, Y. Chen, G. Liu, X. Zhang, J. Sun, Mechanical properties of crystalline Cu/Zr and crystal–amorphous Cu/Cu–Zr multilayers, Mater. Sci. Eng., A 552 (2012) 392–398.
[55] M. Abboud, S. Özerinç, Size-independent strength of amorphous–HCP crystalline metallic nanolayers, J. Mater. Res. 34 (2019) 2275–2284.
[56] K.Y. Yu, Y. Liu, S. Rios, H. Wang, X. Zhang, Strengthening mechanisms of Ag/Ni immiscible multilayers with fcc/fcc interface, Surf. Coating. Technol. 237 (2013) 269–275.

[57] Y.P. Li, X.F. Zhu, G.P. Zhang, J. Tan, W. Wang, B. Wu, Investigation of deformation instability of Au/Cu multilayers by indentation, Philos. Mag. A 90 (2010) 3049–3067.
[58] J. Li, F. Qin, D. Yan, W. Lu, J. Yao, Shear instability in heterogeneous nanolayered Cu/Zr composites, J. Mater. Sci. Technol. 105 (2022) 81–91.
[59] S.P. Wen, R.L. Zong, F. Zeng, Y. Gao, Nanoindentation investigation of the mechanical behaviors of nanoscale Ag/Cu multilayers, J. Mater. Res. 22 (2008) 3423–3431.
[60] F. Wang, P. Huang, M. Xu, T.J. Lu, K.W. Xu, Shear banding deformation in Cu/Ta nano-multilayers, Mater. Sci. Eng., A 528 (2011) 7290–7294.
[61] Y.P. Li, X.F. Zhu, J. Tan, B. Wu, W. Wang, G.P. Zhang, Comparative investigation of strength and plastic instability in Cu/Au and Cu/Cr multilayers by indentation, J. Mater. Res. 24 (2011) 728–735.
[62] B. Cheng, J.R. Trelewicz, Mechanistic coupling of dislocation and shear transformation zone plasticity in crystalline-amorphous nanolaminates, Acta Mater. 117 (2016) 293–305.
[63] N. Bernstein, M.J. Aziz, E. Kaxiras, Amorphous-crystal interface in silicon: a tight-binding simulation, Phys. Rev. B 58 (1998) 4579–4583.
[64] M. Callisti, T. Polcar, Combined size and texture-dependent deformation and strengthening mechanisms in Zr/Nb nano-multilayers, Acta Mater. 124 (2017) 247–260.
[65] R.G. Hoagland, T.E. Mitchell, J.P. Hirth, H. Kung, On the strengthening effects of interfaces in multilayer fcc metallic composites, Philos. Mag. A 82 (2002) 643–664.
[66] J.S. Koehler, Attempt to design a strong solid, Phys. Rev. B 2 (1970) 547–551.
[67] S.I. Rao, P.M. Hazzledine, Atomistic simulations of dislocation–interface interactions in the Cu-Ni multilayer system, Philos. Mag. A 80 (2000) 2011–2040.
[68] W. Cai, V.V. Bulatov, J. Chang, J. Li, S. Yip, Dislocation core effects on mobility, Dislocations in solids 12 (2004).
[69] W.H. Wang, The elastic properties, elastic models and elastic perspectives of metallic glasses, Prog. Mater. Sci. 57 (2012) 487–656.
[70] C. Brandl, T.C. Germann, A. Misra, Structure and shear deformation of metallic crystalline–amorphous interfaces, Acta Mater. 61 (2013) 3600–3611.
[71] C.Q. Chen, Y.T. Pei, J.T.M. De Hosson, Effects of size on the mechanical response of metallic glasses investigated through in situ TEM bending and compression experiments, Acta Mater. 58 (2010) 189–200.
[72] C.A. Volkert, A. Donohue, F. Spaepen, Effect of sample size on deformation in amorphous metals, J. Appl. Phys. 103 (2008), 083539.
[73] D. Jang, J.R. Greer, Transition from a strong-yet-brittle to a stronger-and-ductile state by size reduction of metallic glasses, Nat. Mater. 9 (2010) 215–219.
[74] Y. Zhang, A.L. Greer, Thickness of shear bands in metallic glasses, Appl. Phys. Lett. 89 (2006), 071907.
[75] F. Shimizu, S. Ogata, J. Li, Yield point of metallic glass, Acta Mater. 54 (2006) 4293–4298.
[76] A. Misra, R.G. Hoagland, Plastic flow stability of metallic nanolaminate composites, J. Mater. Sci. 42 (2007) 1765–1771.
[77] T.A. Wynn, D. Bhattacharyya, D.L. Hammon, A. Misra, N.A. Mara, Large strain deformation of bimodal layer thickness Cu/Nb nanolamellar composites, Mater. Sci. Eng., A 564 (2013) 213–217.
[78] Z. Pan, T.J. Rupert, Amorphous intergranular films as toughening structural features, Acta Mater. 89 (2015) 205–214.
[79] W. Cai, V.V. Bulatov, Mobility laws in dislocation dynamics simulations, Mater. Sci. Eng., A 387–389 (2004) 277–281.
[80] W. Pichl, Slip geometry and plastic anisotropy of body-centered cubic metals, Phys. Status Solidi A 189 (2002) 5–25.
[81] C.R. Weinberger, W. Cai, Surface-controlled dislocation multiplication in metal micropillars, Proc. Natl. Acad. Sci. USA 105 (2008) 14304–14307.
[82] S. Brinckmann, J.-Y. Kim, J.R. Greer, Fundamental differences in mechanical behavior between two types of crystals at the nanoscale, Phys. Rev. Lett. 100 (2008), 155502.